The Astronomical Journal, 159:49 (19pp), 2020 February https://doi.org/10.3847/1538-3881/ab5e83

Gravitational Lensing Signatures of Axion Dark Matter Minihalos in Highly Magnified Stars

Liang Dai[1] and Jordi Miralda-Escudé[1,2,3]
[1] School of Natural Sciences, Institute for Advanced Study, 1 Einstein Drive, Princeton, NJ 08540, USA; ldai@ias.edu
[2] Institut de Ciències del Cosmos, Universitat de Barcelona, Martí i Franquès 1, E-08028 Barcelona, Catalonia, Spain
[3] Institució Catalana de Recerca i Estudis Avançats, Passeig Lluís Companys 23, E-08010-Barcelona, Catalonia, Spain
Received 2019 August 5; accepted 2019 December 2; published 2020 January 13

Abstract

Axions are a viable candidate for cold dark matter, which should generically form minihalos of subplanetary masses from white-noise isocurvature density fluctuations if the Peccei–Quinn phase transition occurs after inflation. Despite being denser than the larger halos formed out of adiabatic fluctuations from inflation, axion minihalos have surface densities much smaller than the critical value required for gravitational lensing to produce multiple images or high magnification, and hence are practically undetectable as lenses in isolation. However, their lensing effect can be enhanced when superposed near critical curves of other lenses. We propose a method to detect them through photometric monitoring of recently discovered caustic transiting stars behind cluster lenses, under extreme magnification factors $\mu \gtrsim 10^3$–10^4 as the lensed stars cross microlensing caustics induced by intracluster stars. For masses of the first gravitationally collapsed minihalos in the range $\sim 10^{-15}$–$10^{-8}\, h^{-1}\, M_\odot$, we show that axion minihalos in galaxy clusters should collectively produce subtle surface density fluctuations of amplitude $\sim 10^{-4}$–10^{-3} on projected length scales of $\sim$10–10^4 au, which imprint irregularities on the microlensing lightcurves of caustic transiting stars. We estimate that, inside a cluster halo and over the age of the universe, most of these minihalos are likely to avoid dynamic disruption by encounters with stars or other minihalos.

Unified Astronomy Thesaurus concepts: Cosmology (343); Gravitational lensing (670); Gravitational microlensing (672); Dark matter (353); Galaxy clusters (584)

1. Introduction

Gravitational lensing can reveal self-gravitating objects containing only dark matter (DM), which are difficult to detect by other means because they have expelled or have never accreted baryons. Most DM theories predict the presence of these objects on mass scales much smaller than that of galaxies. Direct detection of these structures would provide crucial clues to the physical origin of DM. A common problem is that these structures are predicted to have surface densities well below the critical value, so they by themselves cannot act as gravitational lenses capable of creating multiple images or inducing substantial image magnifications and distortions, and their effects are often unnoticeable.

However, when these small-scale objects are superposed on a large-scale lens near lensing critical curves, very small surface density perturbations may result in large observable changes (Minor et al. 2017; Dai et al. 2018b). Recently, the first highly magnified stars have been discovered in the field of massive clusters of galaxies (Kelly et al. 2018; Chen et al. 2019; Kaurov et al. 2019). Near the critical curve of the cluster, individual superluminous stars in the background become visible to our most powerful telescopes when magnified by a factor of $\sim 10^2$–10^3. Microlensing by intracluster stars in the lensing cluster introduces fast variability in the magnification (Venumadhav et al. 2017; Diego et al. 2018; Oguri et al. 2018), turning highly magnified stars into a probe not only of the abundance and mass function of intracluster stellar objects, but also of any small-scale density inhomogeneity in the DM.

Axions are a promising DM candidate produced by non-thermal mechanisms in the early universe. As a famous example, the quantum chromodynamics (QCD) axion is motivated by the Peccei–Quinn mechanism (Peccei & Quinn 1977), which explains the absence of a charge-conjugation parity (CP) violating term in the QCD Lagrangian (Weinberg 1978; Wilczek 1978; Kim 1979; Shifman et al. 1980; Dine et al. 1981) as implied by the null value of the neutron electric dipole moment (Pendlebury et al. 2015). Generic axions can arise from other spontaneous broken U(1) symmetries (Chikashige et al. 1981; Gelmini & Roncadelli 1981; Wilczek 1982; Berezhiani & Khlopov 1990; Jaeckel 2014) or from low-energy effective theories emerging from string theory (Georgi et al. 1981; Witten 1984; Conlon 2006; Choi et al. 2009; Cicoli et al. 2012; Dias et al. 2014), and may also account for the DM.

Cosmological models involving axions as the DM predict the existence of very dense, low-mass DM halos through gravitational instability (Hogan & Rees 1988; Kolb & Tkachev 1994) if the Peccei–Quinn symmetry breaking occurs after inflation. However, the surface density of these minihalos would be too low to make them generally detectable through gravitational lensing. Despite a number of proposed lensing methods to detect small-scale axion structures (Kolb & Tkachev 1996; Fairbairn et al. 2017, 2018), so far the range of axion minihalo densities and masses does not seem accessible with any foreseeable observational techniques.

In this paper, we propose the first realistic astrophysical method to detect axion minihalos through gravitational lensing. Highly magnified stars lensed by clusters of galaxies can have apparent fluxes affected by the presence of axion minihalos when they are crossing one of the microcaustics produced by intracluster stars. While the intracluster stars disrupt the cluster critical curve into a network of microcritical curves on angular scales of $\sim 10\ \mu$as, axion minihalos having subplanetary masses and solar system sizes would produce finer magnification variations on much smaller scales of $\sim 10^2$–10^3 nano-arcseconds. When crossing a microcaustic, the observed

lightcurve of a highly magnified star should be altered by surface density fluctuations caused by axion minihalos inside the cluster lens. This paper aims to predict the lensing impacts of axion minihalos on highly magnified stars, which can be monitored through dedicated observations with our most powerful space-borne or ground-based optical and infrared telescopes (Windhorst et al. 2018; Diego 2019).

We outline this work as follows. In Section 2, we start with a review of primordial isocurvature density fluctuations expected to arise from a Peccei–Quinn phase transition in axion DM scenarios. Then, in Section 3, we derive the physical properties of axion minihalos that collapse from primordial isocurvature density fluctuations and show that they are significantly denser and more compact than halos of comparable masses expected in the standard cosmology. In Section 4, we discuss the mass function of axion minihalos. In Section 5, we calculate the size of surface mass density fluctuations due to the cumulative effect of many substructure minihalos along the line of sight through the cluster halo. In Section 6, we estimate the possible dynamic disruption of axion minihalos by mutual encounters or encounters with stars. In Section 7, we study the lensing signatures of axion minihalos imprinted on highly magnified stars and show that sizable irregularities are expected in their lightcurves during microcaustic crossings. Additional discussion is presented in Section 8, and we conclude in Section 9. We discuss some technical details in a few appendices. We use the conventional notation in cosmology wherein many physical quantities are expressed in a way that scales with the dimensionless Hubble parameter h.

2. Isocurvature Density Fluctuations in Axion Cosmology

Axions are a viable particle candidate for nonthermal DM, namely DM that has never interacted substantially with the baryonic matter in the universe since it was created. The axion DM hypothesis is that a global U(1) symmetry of a complex scalar field φ was spontaneously broken in the very early universe (Peccei & Quinn 1977) and gave rise to the axion particle ϕ as the Goldstone mode associated with the angle of φ. If the global U(1) symmetry breaking occurs after inflation during the era of radiation domination, causally disconnected Hubble patches settle down to different vacuum expectation values of ϕ.

The axion can acquire a nonzero mass m_a through nonperturbative effects such as instantons (Gross et al. 1981), which can tilt the potential so that it is no longer flat with respect to ϕ. The axion mass is in general temperature dependent, which induces fluctuations of order unity in the axion field energy density as the field configuration oscillates around the potential minimum $\phi = 0$. This, however, does not occur immediately after the axion acquires its mass because the Hubble timescale is shorter than $\hbar/(m_a\, c^2)$ in the beginning and the axion is dynamically "frozen." During this time, the field configuration is smoothed over the instantaneous horizon scale by the Kibble mechanism (Kibble 1976).

The situation changes when the cosmic expansion eventually slows down to be comparable to the axion field oscillation timescale, $3\,H\,(t_0) \simeq m_a(t_0)c^2/\hbar$. The axion field, which is coherent on the horizon scale at this epoch, $\lambda_H(t_0) \sim c/H(t_0)$, starts to oscillate around $\phi = 0$ and to contribute to the cosmic matter density budget. This generates isocurvature perturbations in addition to the inflationary adiabatic perturbations. The QCD axion starts to oscillate when the universe cools to a temperature $T_0 = T(t_0) \simeq 1.3\,\mathrm{GeV}$ (Buschmann et al. 2019), and the axion mass evolves with the temperature from $m_a(T_0) \sim 6 \times 10^{-9}\,\mathrm{eV}$ to $m_a = 2.5 \times 10^{-5}\,\mathrm{eV}$ at zero temperature (di Cortona et al. 2016; Buschmann et al. 2019), although the exact numbers are subject to theoretical uncertainties (Borsányi et al. 2016). A generic axion particle can have a different mass for which the onset of field oscillation is at a different epoch.

Assuming Gaussian statistics, the total power spectrum for the matter overdensity is the sum of the standard inflationary adiabatic power spectrum $P_{\rm cdm}$ and the axion isocurvature power spectrum $P_{\rm iso}$.[4] At the initial time t_0, the latter can be modeled as a white-noise power spectrum (Hogan & Rees 1988; Fairbairn et al. 2018), $P_{\rm iso}(k) = \Theta(k_0 - k) 24\,\pi^2/(5\,k_0^3)$, where $k_0 = a(t_0)H(t_0)/c$ is a cutoff comoving wavenumber associated with the horizon scale at t_0. Requiring a DM overdensity variance of order unity on the scale k_0 at t_0 fixes the normalization of $P_{\rm iso}$. The total amount of axion mass enclosed within a spherical volume of a comoving radius π/k_0 defines a characteristic mass scale

$$M_0 = (4\,\pi/3)(\pi/k_0)^3\,\bar{\rho}_{a0}, \tag{1}$$

where $\bar{\rho}_{a0}$ is the present-day mean density in axions. This sets the mass scale of the first collapsed objects from the isocurvature perturbations. For the QCD axion, we obtain $M_0 \simeq 5 \times 10^{-10}\,M_\odot$ based on the axion mass parameterization used in Buschmann et al. (2019) and the the effective number of relativistic degrees of freedom presented by Husdal (2016; see Appendix A). After accounting for a factor of $4\pi^4/3 \approx 130$ larger in our definition, this number is compatible with the characteristic masses for the first gravitationally collapsed axion minihalos quoted in other references (Davidson & Schwetz 2016; Hardy 2017; Fairbairn et al. 2018). We therefore estimate that the typical mass for the first collapsed axion minihalos is $\sim 0.01\,M_0$, and is $\sim 5 \times 10^{-12}\,M_\odot$ for QCD axions. For generic axion DM, a wide range of values for M_0 are possible.

The white-noise model is not likely to be a good approximation around the cutoff scale k_0, where the axion field fluctuations are subject to complicated nonlinear dynamics and can be significantly non-Gaussian (Kolb & Tkachev 1996). Numerical simulations find intricate axion clumps on scales shorter than k_0^{-1} (Vaquero et al. 2019; Buschmann et al. 2019). Unrelated to gravitational instability, these clumps emerge soon after the onset of field oscillation at t_0 as a result of complicated Klein–Gordon dynamics, with mass scales as much as four orders of magnitude smaller than the analytic estimate of $\sim 0.01\,M_0$ for the smallest gravitationally collapsed minihalos (Vaquero et al. 2019; Buschmann et al. 2019). These clumps are likely to be contained within the first gravitationally collapsed minihalos, and we distinguish them from axion minihalos, which are the focus of study throughout this paper. The Gaussian white-noise model for minihalos should work well in the shot-noise regime $k \ll k_0$, regardless of the formation of smaller clumps.

With favorable parameter values for the axion cosmology, k_0 typically translates into a length scale many orders of

[4] Throughout the paper, we adopt the simplifying terminology "isocurvature fluctuation" to mean the perturbation in the ratio of the axion density to total density, with a constant baryon-to-photon ratio, which should be distinguished from other forms of isocurvature modes.

magnitude smaller than the range of scales probed through the cosmic microwave background (CMB) anisotropies and the large-scale clustering of galaxies. Therefore, the isocurvature modes that dominate over the adiabatic modes enter the horizon well before the epoch of radiation–matter equality at $z_{\rm eq} \simeq 3400$, so they have wave numbers $k \gg k_{\rm eq} = a(z_{\rm eq})H(z_{\rm eq})/c$. Analytic and numerical calculations of linear perturbations have shown that subhorizon isocurvature matter modes start to grow substantially only when $z > z_{\rm eq}$ (Efstathiou & Bond 1986). Adiabatic modes behave differently during the era of radiation domination: upon entering the horizon, the oscillation of the photon–baryon fluid as an acoustic wave generates an initial peculiar velocity in the DM, leading to a comoving displacement of the DM that grows logarithmically with the scale factor and is responsible for the shape of the linear cold dark matter (CDM) power spectrum at $k > k_{\rm eq}$. In comparison, isocurvature modes induce no such initial peculiar velocities and grow only through the self-gravitation of the DM after horizon entry and the photon–baryon acoustic oscillation (see Appendix B for more details).

Because the white-noise isocurvature power spectrum is only meant to be a crude model, we adopt the approximation that all isocurvature modes grow by the same factor, equal to the usual ΛCDM growth factor $D_+(z)$. We ignore the growth of isocurvature modes at $z < z_{\rm eq}$, noting that this small growth is in any case a nearly constant factor over the relevant range of scales that can be reabsorbed into the definition of k_0. We can then write the linear power spectrum for the total matter overdensity (including both isocurvature and adiabatic modes, but ignoring the gravitational influence of baryons on the isocurvature component) at redshift z as

$$P_m(k, z) = P_{\rm cdm}(k) D_+^2(z) + \Theta(k_0 - k) \times \frac{24\,\pi^2}{5\,k_0^3}\left(\frac{D_+(z)}{D_+(z_i)}\right)^2\left(\frac{1+z_{\rm eq}}{1+z_i}\right)^2. \quad (2)$$

This is valid for $z < z_{\rm eq}$, where z_i is an arbitrarily chosen reference redshift during the era of matter domination satisfying $1 \ll z_i \ll z_{\rm eq}$.

We note that any primordial adiabatic fluctuations of large amplitude and on small scales would be subject to stringent constraints on entropy production from acoustic damping in the primordial plasma (Jeong et al. 2014; Inomata et al. 2016). Because modes of $k \sim 10^2$–$10^8\,h\,{\rm Mpc}^{-1}$ enter the horizon well before the epoch of radiation–matter equality, they would have rapidly dissipated. By contrast, large CDM isocurvature fluctuations are allowed because density fluctuations during the radiation era $z \gg z_{\rm eq}$ are highly suppressed. Neither are these axion isocurvature modes subject to Big Bang nucleosynthesis constraints, which apply to baryonic isocurvature modes of $k \lesssim 10^9\,h\,{\rm Mpc}^{-1}$ (Inomata et al. 2018).

In Figure 1, we plot the total matter overdensity power spectrum linearly extrapolated to $z = 0$ for M_0 in the range 10^{-10}–$10^{-6}\,M_\odot\,h^{-1}$. On comoving scales shorter than the inverse of $k \sim 10^4$–$10^8\,h\,{\rm Mpc}^{-1}$, the isocurvature contribution can dominate the total power. This means that isocurvature perturbations lead to earlier gravitational collapse on those small scales. In fact, on scales $k \sim k_0$, fluctuations are initially of order unity, and they reach nonlinear collapse near the epoch of radiation–matter equality. Note that the sharp reduction of power at scale k_0 in Figure 1 is expected to be smoothed once axion dynamics on scales shorter than k_0 are accurately calculated.

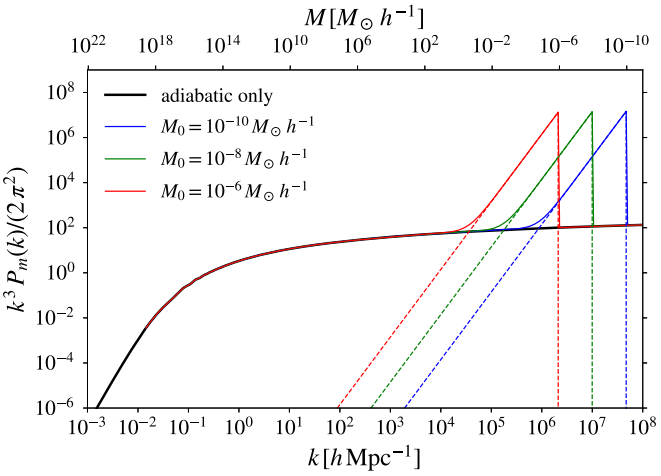

Figure 1. Linear power spectrum of matter overdensity $P_m(k)$ at $z = 0$ assuming all DM is made of axions. The black solid curve shows the standard adiabatic power spectrum, and the colored dashed curves show isocurvature contributions corresponding to various values of M_0. Only isocurvature modes of $k > k_{\rm eq}$, which enter the horizon prior to radiation–matter equality, are shown. For reference, k is converted into a mass scale $M = \bar{\rho}_{a0}(4\pi/3)(\pi/k)^3$ along the top axis.

On sufficiently small scales, gravitational instability is prohibited by the quantum degeneracy pressure of the axion field. The comoving wavenumber of the effective Jeans scale is given by (Fairbairn et al. 2018)

$$k_J = (16\,\pi\,G\,a\,\bar{\rho}_{a0})^{1/4}(m_a/\hbar)^{1/2} = 6.7\times10^{10}\,{\rm Mpc}^{-1}(1+z)^{-1/4} \times\left(\frac{\Omega_m h^2}{0.12}\right)^{1/4}\left(\frac{m_a}{10^{-4}\,{\rm eV}}\right)^{1/2}. \quad (3)$$

Structure formation becomes efficient at $z < z_{\rm eq} \simeq 3400$, and the expected QCD axion has a mass in the range $m_a \sim 10^{-6}$–10^{-4} eV at zero temperature, so Equation (3) suggests that quantum degeneracy pressure is negligible for the gravitational instability of the isocurvature modes shown in Figure 1.

3. Size and Density of Axion Minihalos

During the epoch of matter domination, collapsed objects form after the matter overdensity amplitude reaches a value near unity. Around the epoch of radiation–matter equality, the first collapsed objects form on a comoving scale $\sim 1/k_0$ with masses $\sim 0.01\,M_0$. Similar to that in the standard cosmology, hierarchical assembly of collapsed objects proceeds in a bottom-up fashion toward larger length scales (and smaller comoving wave numbers). Increasingly larger halos are built up from mergers of smaller ones and accretion of smooth matter, and they develop an internal structure of orbiting satellite halos, with at least a fraction of them surviving dynamical disruption. This structure may have multiple levels of orbiting satellites within orbiting satellites. The hierarchical process takes place first during $z_{\rm eq} > z \gtrsim 20$ on very small scales, where the white-noise isocurvature power spectrum dominates. Then, at $z \lesssim 20$, the inflationary adiabatic power spectrum is dominant, and structure formation proceeds in a way identical to that of the standard CDM cosmology, except

that a fraction of the DM is clumped in the form of vast numbers of very small and dense orbiting minihalos.

Consider the collapse of a spherical region at redshift $z_{\rm coll}$, which has a comoving Lagrangian radius R and an enclosed mass $M = (4\pi/3)\bar{\rho}_{a0} R^3$. Exact spherical symmetry in collapse is unrealistic for predicting the correct density profile of the collapsed halos. Numerical studies of collapse from Gaussian random overdensities using N-body simulations suggest that halos formed through hierarchical assembly in general follow the phenomenological Navarro–Frenk–White (NFW) density profile (Navarro et al. 1996, 1997) $\rho(r) = \rho_s/[(r/r_s)(1 + r/r_s)^2]$, which is defined by a scale density ρ_s and a scale radius r_s.

The literature on CDM halos has commonly used three quantities to characterize an NFW halo: the virial mass M_{200}, the virial radius r_{200}, and the concentration parameter $c_{200} = r_{200}/r_s$. Instead, we treat ρ_s and r_s as fundamental parameters that are closely tied to the time of halo collapse. Numerical studies suggest a "two-step" picture for the formation and evolution of halos (especially at low peak heights): upon collapse, the halo first undergoes a phase of rapid growth to reach a typical concentration factor $c_\star \simeq 4$ (Zhao et al. 2003, 2009); after that, halo growth slows down while its inner profile stabilizes (Bullock et al. 2001; Ludlow et al. 2013). During the second phase, which is often referred to as pseudo-evolution, ρ_s and r_s hardly change if measured in proper units, while the virial mass and the virial radius still increase due to mass accretion onto the outer parts. The picture of pseudo-evolution applies particularly well to isolated halos that grow slowly from the low-density surrounding material, which are typically of low mass compared to the characteristic collapsing mass at each epoch. Using ρ_s and r_s is convenient for quantifying the gravitational lensing effect; they characterize the halo's inner region, which is much denser and more compact than the entire virialized region at high halo concentration. We therefore describe NFW halos using ρ_s and r_s, assumed to be stationary from the onset of the pseudo-evolution phase.

The linear matter overdensity smoothed over a scale R has a variance $\sigma^2(M, z) = \int d\ \ln k\ [k^3 P_m(k, z)]/(2\pi^2)|W(k, R)|^2$, where $W(k, R) = 3(kR)^{-3}\,[\sin(kR) - (kR)\cos(kR)]$ is the spherical top-hat window function. At each redshift, one can derive the mass scale M and the comoving radius scale $R = R(M)$ that collapse from any given peak height $\nu(M, z) = \delta_c/\sigma(M, z)$, where $\delta_c = 1.686$ is the threshold overdensity during the era of matter domination. Halos of mass M collapse over a broad range of redshifts, but we can define a universal median collapse redshift corresponding to a fluctuation with $\nu = \nu_{\rm med} = 0.67$. For any M, a characteristic mass-dependent collapse redshift $z_{\rm coll}(M)$ follows by solving $\nu_{\rm med} = \delta_c/\sigma(M, z_{\rm coll})$. When isocurvature fluctuations dominate the overdensity power spectrum in Equation (2), the median collapse redshift is derived to be

$$1 + z_{\rm coll}(M) = (18/5\,\pi^2)^{1/2}(\nu_{\rm med}/\delta_c)(1 + z_{\rm eq})(M_0/M)^{1/2} = 0.24(1 + z_{\rm eq})(M_0/M)^{1/2}. \quad (4)$$

To estimate the NFW fundamental parameters, we assume that the collapsed NFW halo has a universal concentration parameter $c_\star = r_{200}/r_s = 4$, its enclosed mass within r_{200} equals M, and the mean density within r_{200} is 200 times the cosmic mean $\bar{\rho}_a(z_{\rm coll}) = \bar{\rho}_{a0}(1 + z_{\rm coll})^3$. For $c_\star = 4$, we find $\rho_s \approx 5271\ \bar{\rho}_a(z_{\rm coll})$, $r_s \approx 0.0265\ [M/\bar{\rho}_a(z_{\rm coll})]^{1/3}$, and $M \approx 10.2\ \rho_s r_s^3$. When the white-noise isocurvature power spectrum dominates, the resultant halos, which we refer to as minihalos, obey the following scaling relations with the mass scale M,

$$\rho_s(M) \approx 0.24\ M_\odot\ h^2\ /{\rm pc}^3 \left(\frac{\nu}{\nu_{\rm med}}\right)^3 \frac{\Omega_a}{0.3}\left(\frac{1 + z_{\rm eq}}{3400}\right)^3 \times \left(\frac{M_0}{10^{-10}\,M_\odot\,h^{-1}}\right)^{3/2}\left(\frac{M}{10^{-6}\,M_\odot\,h^{-1}}\right)^{-3/2}, \quad (5)$$

and

$$r_s(M) \approx 1530\ h^{-1}\ {\rm au}\left(\frac{1 + z_{\rm eq}}{3400}\,\frac{\nu}{\nu_{\rm med}}\right)^{-1}\left(\frac{\Omega_a}{0.3}\right)^{-1/3} \times \left(\frac{M_0}{10^{-10}\,M_\odot\,h^{-1}}\right)^{-1/2}\left(\frac{M}{10^{-6}\,M_\odot\,h^{-1}}\right)^{5/6}. \quad (6)$$

It is useful at this point to compare the characteristic surface density of axion minihalos, $\rho_s(M)r_s(M)$, with the critical surface density in gravitational lensing, required for an isolated lens to produce multiple images and high magnification. The critical surface density is given by $\Sigma_{\rm crit} = c^2/(4\pi G D_{\rm eff})$, where $D_{\rm eff} = D_L D_{LS}/D_S$ for angular diameter distances D_L to the lens, D_S to the source, and D_{LS} from the lens to the source. The typical lensing convergence of an axion minihalo near the scale radius, $\kappa_s(M) \approx \rho_s(M)r_s(M)/\Sigma_{\rm crit}$, is tiny,

$$\kappa_s(M) \approx 7 \times 10^{-7}\,\frac{D_{\rm eff}}{1\ {\rm Gpc}}\left(\frac{\nu}{\nu_{\rm med}}\right)^2\left(\frac{\Omega_a}{0.3}\right)^{2/3} \times \left(\frac{1 + z_{\rm eq}}{3400}\right)^2\left(\frac{M_0}{10^{-10}\,M_\odot\,h^{-1}}\right)\left(\frac{M}{10^{-6}\,M_\odot\,h^{-1}}\right)^{-2/3}. \quad (7)$$

Even for dense minihalos with $M = 10^{-10}\,M_\odot\,h^{-1}$, acting as individual lenses at cosmological distances, $\kappa_s(M)$ is no greater than $\sim 10^{-3}$. Axion minihalos can therefore not produce substantial lensing effects by themselves, but we will show in this paper that they can be detected when acting in conjunction with a galaxy cluster lens and intracluster stars near a lensing critical curve.

In Figure 2, we check whether the above simple peak-height prescription gives reasonably good estimates for the fundamental parameters ρ_s and r_s of halos at low masses. We first generate random NFW halos in the standard ΛCDM cosmology within a range of redshifts $0 < z < 15$ and a range of virial masses $-16 < \log(M_{200}\,h/M_\odot) < 10$ sampled from N-body simulations (Diemer & Joyce 2018). Next, we calculate their r_s and ρ_s using a number of median concentration–mass relations from the literature, which are empirically calibrated to simulations. When we scatter-plot the halos on the (r_s, ρ_s) plane, they all lie within a squeezed band, which is particularly narrow at very small halo masses. This indicates that the notion of pseudo-evolution is reasonably valid for low-mass halos. For a comparison, we then analytically estimate the ρ_s and r_s of median halos using the peak-height prescription: we identify peaks with a median height $\nu = \nu_{\rm med}$ at various redshifts, and then calculate using the relations $\rho_s \approx 5271\ \bar{\rho}_a(z_{\rm coll})$ and

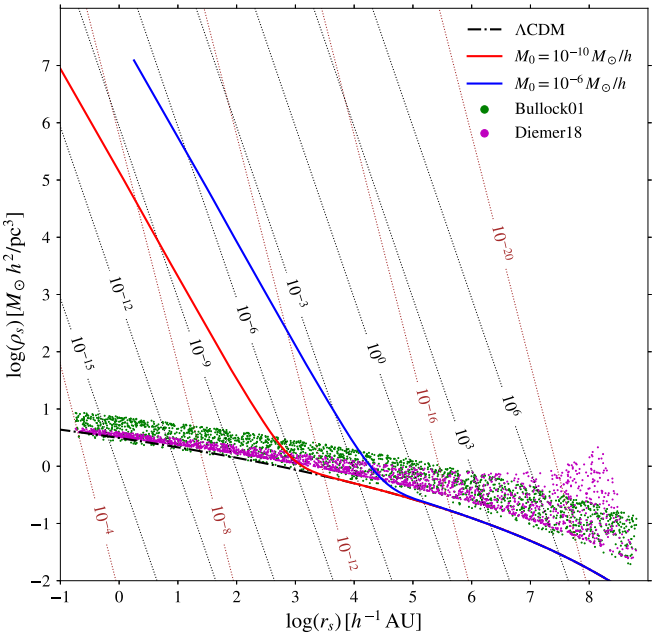

Figure 2. Scale radius r_s vs. scale density ρ_s for NFW halos in standard or axion cosmologies. We scatter-plot r_s and ρ_s for standard CDM halos drawn from $0 < z < 15$ and $-16 < \log(M_{200}\,h/M_\odot) < 10$ assuming the median halo concentration–mass relation from Bullock et al. (2001, green dots) and from Diemer & Joyce (2018, magenta dots). Curves show r_s and ρ_s calculated from the simple prescription that a spherical top-hat region enclosing mass M with a median peak height $\nu = \nu_{\rm med} = 0.67$ collapses into an NFW halo with concentration $c_{200} = r_{200}/r_s = 4$ and mass M within r_{200}. The black dashed–dotted curve is for standard ΛCDM cosmology. Blue ($M_0 = 10^{-10}\,M_\odot\,h^{-1}$) and red ($M_0 = 10^{-6}\,M_\odot\,h^{-1}$) curves are computed using the axion cosmology power spectrum Equation (2). Black dotted contours show $10.2\,\rho_s\,r_s^3$ in units of $M_\odot h^{-1}$. Brown dotted contours show the axion mass m_a below which quantum degeneracy pressure is dynamically important, in units of eV · h.

$r_s \approx 0.0265\,[M/\bar{\rho}_a(z_{\rm coll})]^{1/3}$, where at any given collapse redshift $z_{\rm coll}$ we solve the top-hat mass M from $\nu(M,\,z_{\rm coll}) = \delta_c/\sigma(M,\,z_{\rm coll}) = \nu_{\rm med}$. On the $(r_s,\,\rho_s)$ plane, this produces a single curve parameterized by the collapse redshift $z_{\rm coll}$ or alternatively the top-hat mass M. At small halo masses, this curve aligns reasonably well with the narrow band of halos identified from numerical simulations.

With this justification, hereafter we rely on the above peak-height prescription to estimate halo size and density in axion cosmology. We show some sample curves in Figure 2. We see that in axion cosmology, sufficiently small halos can be many orders of magnitude denser than their ΛCDM counterparts (Diemand et al. 2005; Berezinsky et al. 2006; Diemand et al. 2006).

The inner region of the collapsed axion halo has a typical de Broglie wavelength $\lambda_{\rm dB} = (2\,\pi\,\hbar)/(m_a\,\sigma)$, where we estimate velocity dispersion as $\sigma \sim (G\,\rho_s\,r_s)^{1/2}$. The quantum degeneracy pressure is dynamically unimportant if $\lambda_{\rm dB} \ll r_s$, which requires

$$m_a > \left[\frac{(2\,\pi\,\hbar)^2}{G\,\rho_s\,r_s^4}\right]^{1/2} \approx 8\times10^{-12}\,\mathrm{eV}\,h \times\left(\frac{\rho_s}{10^4\,M_\odot\,h^2\,\mathrm{pc}^{-3}}\right)^{-1/2}\left(\frac{r_s}{10^2\,h^{-1}\,\mathrm{au}}\right)^{-2}. \quad (8)$$

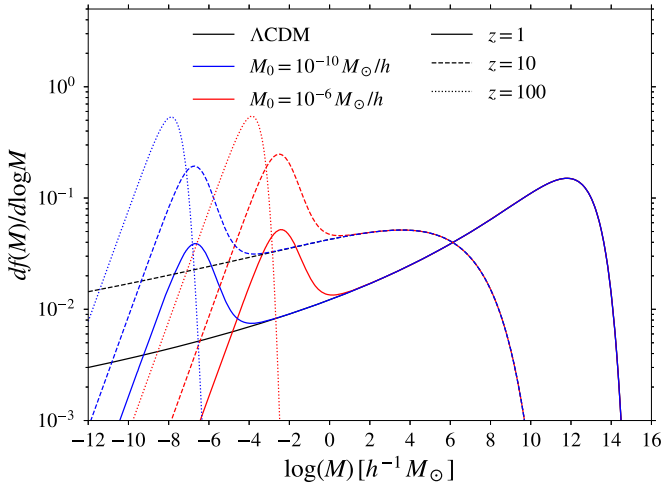

Figure 3. Differential mass fractions of isolated collapsed halos, $df\,(M)\,/d\,\log M$, computed from the Press–Schechter formalism. We compare the standard CDM cosmology (black) and the axion cosmology with two different values for the M_0 parameter, $10^{-10}\,h^{-1}M_\odot$ (blue) and $10^{-6}\,h^{-1}M_\odot$ (red), at three different redshifts: $z = 1$ (solid), $z = 10$ (dashed), and $z = 100$ (dotted).

Whenever this is valid, the axion halo can be modeled as a self-gravitating system made of classical collisionless particles (if axion self-interaction is negligible). In Figure 2, we overplot contours for this minimum axion mass, such that for any given value of m_a, halos located on the upper-right side of the contour on the $(r_s,\,\rho_s)$ plane are not dynamically affected by the degeneracy pressure. For the mass range $m_a \sim 10^{-6}$–10^{-4} eV (at zero temperature) which brackets the theoretically favorable mass for the QCD axion, axion minihalos formed from isocurvature fluctuations are not affected by the degeneracy pressure.

4. Mass Function of Axion Minihalos

The Press–Schechter (PS) formalism (Press & Schechter 1974) predicts that at a given time t, the collapsed halos have a mass function $n(M,\,t) = (\bar{\rho}_m(t)/M^3)df\,(M,\,t)/d\,\ln M$. We define $n(M,\,t)$ to be the proper volume number density of halos per logarithmic interval of mass M. The mass fraction per logarithmic interval of mass is

$$\frac{df\,(M,\,t)}{d\,\ln M} = \sqrt{\frac{2}{\pi}}\,\nu(M,t)\exp\left(-\frac{\nu^2(M,\,t)}{2}\right)\left|\frac{\partial\ln\sigma(M,\,t)}{\partial\ln M}\right|. \quad (9)$$

Here, $\bar{\rho}_m(t)$ is the mean matter density and $\nu(M,\,t) = \delta_c/\sigma(M,\,t)$ is the peak height.

The PS mass function excludes small halos that have been incorporated into larger ones as subhalos. Some subhalos are disrupted, while others may survive for long. Both isolated halos and subhalos act as perturber lenses, so as far as gravitational lensing is concerned; Equation (9) sets a lower limit to the fraction of mass locked up in collapsed, dense objects.

In Figure 3, we adopt the PS formalism to compute $df/d\,\log M$ at various redshifts. We consider different values of M_0 for the axion cosmology and compare the results to those of standard cosmology. As an example, for $M_0 = 10^{-10}\,h^{-1}\,M_\odot$, by $z = 100$, virtually all DM is locked up in

collapsed axion minihalos of masses $M < 10^{-6}\,h^{-1}\,M_{\odot}$, well before any galactic-scale halos form. As hierarchical assembly proceeds, small minihalos gradually assemble into larger halos. By $z = 10$, about 50% of DM resides in isolated minihalos of masses $M < 10^{-4}\,h^{-1}\,M_{\odot}$, and a substantial fraction has already assembled into the first dwarf-galaxy halos from the nonlinear collapse of adiabatic fluctuations. By $z = 1$, around the time when the most massive galaxy clusters are forming, isolated minihalos of masses $M < 10^{-4}\,h^{-1}M_{\odot}$ still contribute about 10% of all DM. This provides a lower limit on the mass budget of minihalos of $M < 10^{-4}\,h^{-1}M_{\odot}$ in the universe, because we have excluded subhalos of similar masses whose contribution depends on the substructure survival fraction and is not accounted for by the PS formalism.

Figure 3 shows that structure formation in axion cosmology differs substantially from that in standard cosmology because the collapse times of the very low-mass halos shift to earlier epochs. In standard cosmology, practically no DM structures have collapsed on any scales by $z = 100$. The lowest-mass halos form only at $z \sim 20$, at an epoch not well separated from the formation times of the first halos of dwarf-galaxy scale. For the axion cosmology with $M_0 = 10^{-10}\,h^{-1}M_{\odot}$, isolated halos with $M \lesssim 10^{-4}\,h^{-1}M_{\odot}$ account for ∼30% of all DM. By $z = 1$, this fraction drops to ∼10% as more of them merge into larger halos. On the other hand, the DM mass fraction (including substructure) residing in large halos converges between the standard cosmology and the axion cosmology. The PS calculation indicates that in axion cosmology, the mass fraction in tiny isolated minihalos with $M < 10^{-4}\,h^{-1}M_{\odot}$ is much higher than that in standard cosmology. Moreover, the low-mass axion minihalos are much denser, so they are much more likely to survive as substructure when they merge into larger halos. When the value of M_0 is increased, for example, to $M_0 = 10^{-6}\,h^{-1}M_{\odot}$, the characteristic minihalo masses shift to larger masses; the aforementioned conclusions remain qualitatively true after numbers are appropriately rescaled.

The PS calculation includes only isolated minihalos, whereas observations of caustic transiting stars behind lensing clusters are predominantly probing DM subhalos inside galaxy clusters rather than intervening field halos in intergalactic space (see discussion in Section 5). Nevertheless, we make the following argument to translate the above results to the subhalo mass fraction inside a galaxy cluster, up to caveats regarding minihalos surviving dynamic disruption in the intracluster environment. Most of the mass of a galaxy cluster accretes at $z \sim 1$ from the intergalactic medium, where the abundance of small DM halos shortly before the accretion to the cluster is well described by the PS mass function. Being much denser than the cluster halo, the axion minihalos are unlikely to be disrupted once they merge into the cluster. The fractional mass function of minihalos inside the cluster halo can therefore be approximately described by Equation (9). This approximation is still a lower limit to the number of minihalos, because the PS formalism does not include minihalos that collapse and survive as subhalos in intermediate-mass halos, and are incorporated into the cluster when the intermediate-mass object merges into the cluster.

Using this justification, we will use Equation (9) to estimate the power spectrum of the surface density projected along the line of sight through a cluster halo in Section 5. The various theoretical uncertainties regarding dynamical disruption of minihalos and the multiple levels of subhalos inside subhalos will affect our result only by a moderate factor reflecting the fraction of DM in axion minihalos.

5. Cumulative Effect of Minihalos along a Line of Sight

The main goal of this paper is to analyze the gravitational lensing impact of axion minihalos in the line of sight to a source observed at high magnification. As mentioned, axion minihalos are difficult to detect with gravitational lensing because of their low surface density. However, small surface density fluctuations $\Delta\Sigma$ produce large effects near critical curves, when the lensing magnification is as high as $\sim\Sigma_{\rm crit}/\Delta\Sigma$.

Near the critical curve of a galaxy cluster, the total cluster surface density is close to $\Sigma_{\rm crit}$, whereas the surface density of an individual minihalo is much lower. This implies that if, as argued above, axion minihalos contain a substantial fraction of all the DM, their area covering factor is much larger than unity. Therefore, axion minihalos must move through each other on many high-speed encounters as they orbit inside the cluster halo. At the same time, surface density fluctuations near a lensing critical curve result from the superposition of many axion minihalos, and can therefore be treated as a Gaussian random field, with all the information being included in the power spectrum. We evaluate the surface density power spectrum in this section.

5.1. Surface Density Power Spectrum

A useful starting point of the calculation is to consider that all the relevant density fluctuations are contained in a statistically homogeneous slab of thickness L, which is much larger than any transverse scales of interest. As shown in Appendix C, the power spectrum of the surface density field Σ is in this case related to that of the volumetric density field ρ as $P_{\Sigma}(q_{\perp}) = P_{\rho}(q_{\perp})L$, where $q_{\perp}$ is the two-dimensional Fourier wavenumber conjugate to the transverse length scale in proper units. This also assumes that the power spectrum is not too blue, obeying $d\,\ln P_{\rho}(q)/d\,\ln q < 1$, where q denotes the three-dimensional Fourier wavenumber.

If all mass were locked into subhalos of some mass M and number density per unit $\ln M$ given by $n(M) = (\bar{\rho}/M)df(M)/d\,\ln M$, the volumetric density power spectrum is (see Cooray & Sheth 2002),

$$P_{\rho}(q) = \int d\,\ln M\, n(M)|\tilde{\rho}^{(h)}(q;M)|^2 = \bar{\rho}\int \frac{dM}{M^2}\frac{df(M)}{d\,\ln M}|\tilde{\rho}^{(h)}(q;M)|^2. \quad (10)$$

where $\bar{\rho}$ is the mean density, and

$$\tilde{\rho}^{(h)}(q;M) \equiv 4\pi\int_0^{\infty} r^2\,dr\,\frac{\sin(q\,r)}{q\,r}\,\rho^{(h)}(r;M) \quad (11)$$

is the Fourier transform of the halo density profile (assumed to be spherically symmetric) at halo mass M. In principle, the subhalo mass distribution does not have to be the same as the field distribution in Equation (9) considered in the previous section, but by the argument put forward in Section 4, we will use the approximation here that they are the same.

We now consider a long slab along the line of sight through the cluster halo. The total length of the slab is of the order of the cluster virialization scale ∼Mpc. The scale of the relevant transverse modes is comparable to the radii of the axion

minihalos, which is orders of magnitude smaller. Because the coarse-grained density profile varies substantially from the inner region to the outer region of the cluster halo, it is invalid to assume that the volumetric density field is statistically homogeneous when deriving the power spectrum of the surface density field across the slab. Therefore, we divide the slab along the line of sight into many subslabs. Each subslab is sufficiently thin for the density field to have approximately homogeneous statistics, but is thick enough for the derivation of Appendix C to be valid. The surface density field through the entire slab has a power spectrum equal to the uncorrelated sum of the contributions from all subslabs.

We make another simplifying premise that all subslabs share the same fractional mass distribution as a function of halo mass, $df/d\ln M$. Then, the halo mass function is linearly proportional to the local mean density in each subslab. According to Equation (10), the power spectrum for the surface density field is given by a summation over all subslabs, or an integral along the line of sight in the limit of a large number of subslabs,

$$P_\Sigma(q_\perp) = \left(\int \frac{dM}{M^2}\frac{df(M)}{d\ln M}\,|\tilde{\rho}^{(h)}(q_\perp; M)|^2\right)\left(\int dL\,\overline{\rho}(L)\right) = \overline{\Sigma}\left(\int \frac{dM}{M^2}\frac{df(M)}{d\ln M}\,|\tilde{\rho}^{(h)}(q_\perp; M)|^2\right), \tag{12}$$

where $\int dL(\cdots)$ is the line-of-sight integral. The fractional surface overdensity, defined as $\delta_{2d} \equiv \Sigma/\overline{\Sigma}$, has a power spectrum

$$P_{\delta_{2d}}(q_\perp) = \frac{1}{\overline{\Sigma}}\left(\int \frac{dM}{M^2}\frac{df(M)}{d\ln M}\,|\tilde{\rho}^{(h)}(q_\perp; M)|^2\right). \tag{13}$$

Under our assumptions, only the mean surface density $\overline{\Sigma}$ is needed for computing $P_{\delta_{2d}}(q_\perp)$, provided that the (uniform) fractional mass distribution $df/d\ln M$ and the halo density profiles are known.

Apart from minihalos residing in the cluster halo, intervening minihalos freely floating in intergalactic space are also expected. Indeed, in substructure tests utilizing galaxy-scale lensing, intervening field halos integrated over a cosmological distance can be equally important or even dominant compared to subhalos (Despali et al. 2018). By comparison, the amount of substructure through a rich galaxy cluster is substantially larger. Assuming similar mass fractions of minihalos inside the cluster halo and in intergalactic space, the relative importance of the two contributions can be inferred from comparing the surface density through the cluster $\overline{\Sigma}_{\rm cl}$ and the integrated DM surface density everywhere else along the line of sight $\overline{\Sigma}_{\rm los}$. For the two known highly magnified stars behind MACS J1149 (Kelly et al. 2018) and behind MACS J0416 (Chen et al. 2019; Kaurov et al. 2019), we find $\overline{\Sigma}_{\rm los} \approx 0.1$–$0.2\,\overline{\Sigma}_{\rm cl}$, which indicates that intergalactic minihalos should be subdominant.

It is convenient to measure the surface mass density in units of $\Sigma_{\rm crit}$, which gives the lensing convergence $\kappa = \Sigma/\Sigma_{\rm crit}$. Ignoring intergalactic minihalos, the lensing convergence has a power spectrum

$$P_\kappa(q_\perp) = \frac{\overline{\Sigma}_{\rm cl}}{\Sigma_c^2}\int \frac{dM}{M^2}\frac{df(M)}{d\ln M}\,|\tilde{\rho}^{(h)}(q_\perp; M)|^2. \tag{14}$$

We emphasize that this calculation is conservative because it only counts minihalos formed in isolation prior to cluster formation and excludes minihalos who themselves orbit intermediate-mass subhalos (i.e., subhalos of subhalos).

In Figure 4, we present a calculation of the convergence power spectrum for the specific case of the line of sight toward the highly magnified star LS1 behind MACS J1149. In the calculation, we assume that axion minihalos inside the cluster halo obey the PS mass function, Equation (9), but ignore additional contributions to the clumpy surface density, due to those minihalos having their own satellite minihalos.

In the left panel of Figure 4, we compute $\Delta_\kappa(q_\perp) \equiv [q_\perp^2\,P_\kappa(q_\perp)/(2\pi)]^{1/2}$, which quantifies the characteristic fluctuation in the lensing convergence κ as a function of the transverse length scale. For $M_0 = 10^{-10}\,M_\odot\,h^{-1}$, κ can fluctuate at the level of $\Delta_\kappa \sim 10^{-4}$ on scales $r_\perp = (2\pi)/q_\perp = 10$–$10^4$ au h^{-1}, which, as we will explain in Section 7, are probed by the lightcurves of the highly magnified stars during events of microlensing peaks. The right panel of Figure 4 shows that at a fixed wavenumber $q_\perp$, the convergence fluctuation originates mainly from minihalos with a typical scale radius $r_s \simeq r_\perp = (2\pi)/q_\perp$.

For an increased value for the parameter $M_0 = 10^{-6}\,M_\odot\,h^{-1}$, axion minihalos of $M \lesssim 10^{-2}\,M_\odot\,h^{-1}$ form earlier and thus are more compact. As a result, the typical convergence fluctuation on those scales can increase to $\Delta_\kappa \sim 10^{-3}$. If instead M_0 is several orders of magnitudes smaller, axion minihalos in the mass range of our interest become less dense, and the resultant convergence fluctuation is reduced.

The left panel of Figure 4 indicates convergence fluctuations at the level of $\Delta_\kappa \sim 10^{-4}$–$10^{-3}$ for a broad range $M_0 = 10^{-13}$–$10^{-6}\,M_\odot\,h^{-1}$, which translates into the mass scale of the earliest gravitational collapse $\sim 0.01\,M_0 = 10^{-15}$–$10^{-8}\,M_\odot\,h^{-1}$. The results are not very sensitive to the choice of the cluster formation redshift z_f at which the PS mass function is evaluated.

5.2. Area Covering Factor

Assuming a uniform $df/d\ln M$ throughout the cluster halo, we can calculate the optical depth to intersecting a minihalo of mass M within the scale radius $r_s(M)$. Taking a geometric cross section πr_s^2, the differential optical depth is

$$\frac{d\tau(M)}{d\ln M} = \frac{\pi\,r_s^2(M)\,\overline{\Sigma}_{\rm cl}}{M}\frac{df(M)}{d\ln M}. \tag{15}$$

This can be interpreted as the area covering factor.

Figure 5 plots this optical depth as a function of the halo mass, for $M_0 = 10^{-10}$ and $10^{-6}\,M_\odot\,h^{-1}$, respectively. Taking $M_0 = 10^{-10}\,M_\odot\,h^{-1}$ as the example, we find that minihalos formed from isocurvature density fluctuations $M \sim 10^{-10}$–$10^{-6}\,M_\odot\,h^{-1}$ generally have $d\tau/d\log M \gg 1$. Within this mass range, as increasingly massive (and hence physically bigger) minihalos are considered, a single line of sight traversing the entire cluster halo intersects an increasingly larger number of minihalos. Because these minihalos are the major contributors to convergence fluctuations on scales of $\sim$10–10^4 au h^{-1}, the convergence field, by the central limit theorem, is locally well described by a Gaussian random field with an isotropic power spectrum Equation (14). The supercritical area covering fraction for axion minihalos is in sharp contrast to their volume occupation fraction, which is tiny because of the characteristic density of

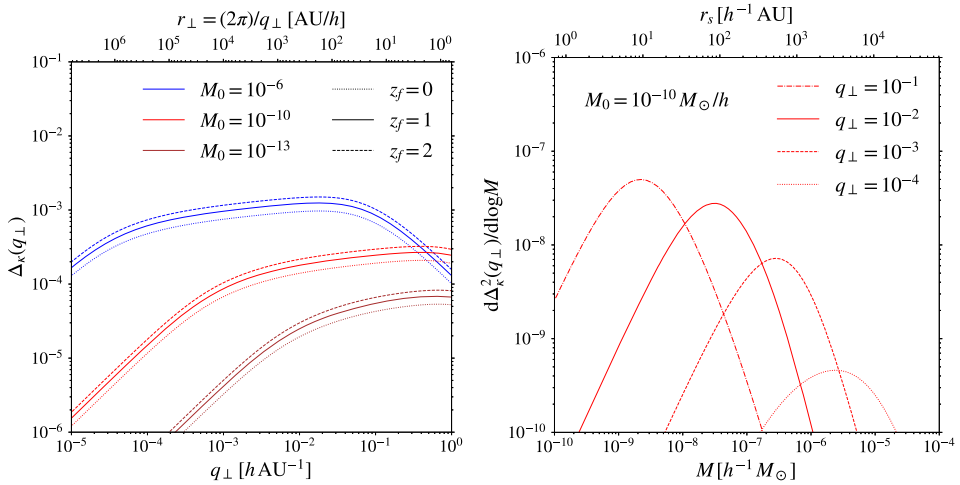

Figure 4. The case of the line of sight to the caustic-straddling lensed galaxy behind the lensing cluster MACS J1149. Left panel: characteristic fluctuation $\Delta_\kappa(q_\perp)$ in the convergence κ as a function of the projected Fourier wavenumber $q_\perp$. When evaluating the PS mass function $df/d\ln M$ (see Equation (9)), we set the redshift $z_f = 0$ (dotted), 1 (solid), and 2 (dashed). We plot curves for three different values for the axion cosmology characteristic mass scale (in units of $M_\odot h^{-1}$) $M_0 = 10^{-6}$ (blue), 10^{-10} (red), and 10^{-13} (brown). The top axis indicates the corresponding projected proper length scale $r_\perp = 2\pi/q_\perp$. Right panel: differential contribution to the variance of the convergence from axion minihalos of different masses at a given $q_\perp$. We set $M_0 = 10^{-10}\,M_\odot h^{-1}$, and show curves for $q_\perp = 10^{-1}$ (dashed–dotted), 10^{-2} (solid), 10^{-3} (dashed) and 10^{-4} (dotted), all in units of h au^{-1}. The top axis indicates the corresponding minihalo-scale radius r_s. Calculations exclude subhalos inside subhalos.

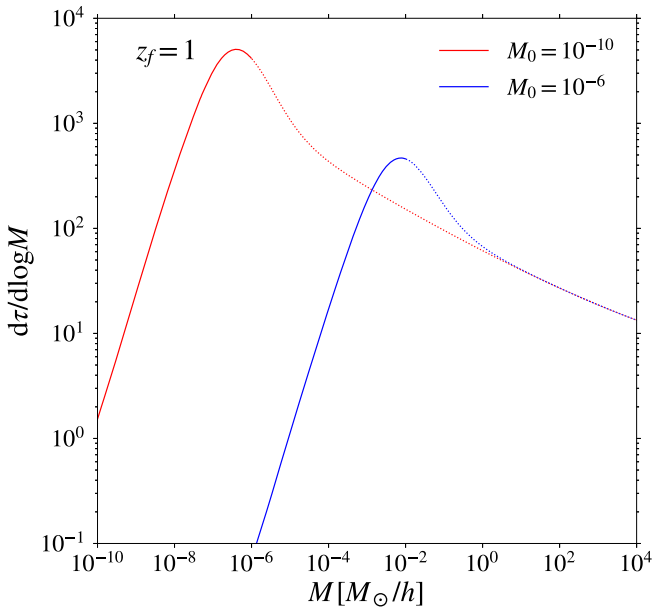

Figure 5. Differential area covering fraction $d\tau/d\log M$ for axion minihalos of a range of masses (Equation (15)). We consider two values for the axion cosmology characteristic mass scale $M_0 = 10^{-10}\,M_\odot h^{-1}$ (red) and $10^{-6}\,M_\odot h^{-1}$ (blue). For each curve, the left portion (solid) corresponds to halos that form from isocurvature density fluctuations, and the right portion (dotted) corresponds to halos that form from adiabatic density fluctuations.

minihalos being many orders of magnitude higher than that of the cluster halo.

As for the more massive halos $M \gtrsim 10^{-6}\,M_\odot h^{-1}$ formed from the adiabatic density fluctuations, the area covering factor starts to decrease. That part of the curve is shown as dotted, because the area covering factor is certainly overestimated toward larger M. Applying the PS mass function $df/d\ln M$ to intracluster substructures severely overestimates the abundance of those halos inside the cluster halo as simulations suggest that many of them do not survive disruption. This is because the density hierarchy between those halos and the cluster halo is substantially narrower, and because across several decades of masses those halos collapse at similar redshifts and therefore all have similar densities (Diemand et al. 2006). It should be clear to readers that those halos are not the focus of this study.

In the case of $M_0 = 10^{-6}\,M_\odot h^{-1}$, we reach a similar conclusion for minihalos of masses $M \sim 10^{-4}$–$10^{-2}\,M_\odot h^{-1}$, although the overlap in projection for the least massive minihalos ($M \lesssim 10^{-4}\,M_\odot$) are not high enough to render the convergence field completely Gaussian. Finally, we note that our evaluation of Equation (15) has left out minihalos inside subhalos or minihalos into higher levels of substructure hierarchy. Including those will further Gaussianize the convergence field and increase its power spectrum.

6. Dynamical Disruption of Minihalos inside Clusters

We now discuss the dynamical processes that determine the survival rate of axion minihalos orbiting within larger CDM halos. We consider minihalos of mass m_1 and radius r_1 orbiting within a parent halo of mass M and radius R. Those account for a fraction of the total host halo mass $df_{\rm sub}(m_1; M)/d\ln m_1$. We distinguish this from the PS mass fraction $df(m_1)/d\ln m_1$, which neither accounts for the dynamic destruction of subhalos, nor for the fact that minihalos of mass m_1 exist at multiple levels of substructure hierarchy (subhalos of subhalos, and so on), all of which participate in dynamical processes.

We discuss three important dynamical processes that determine the destruction rate of minihalos:

1. Spiraling to the host halo center by dynamical friction, and tidal disruption at the high central halo mass density (which may be enhanced by baryonic processes in galactic centers such as disk and bulge formation).
2. Dynamical heating during high-speed encounters with other minihalos.
3. Dynamical heating during high-speed encounters with baryonic structures, including stars and molecular clouds.

We will show that among these destruction mechanisms, the most important is the second one if only DM is present, and the

third one after stars have formed. Our estimates suggest that, over the age of the universe, minihalos of our concern are unlikely to be disrupted by a significant fraction in a typical galaxy cluster when stars in member galaxies are taken into account. Some useful order-of-magnitude formulae are collected in Appendix D.

6.1. Dynamical Friction and Tidal Disruption near the Halo Center

For a subhalo of mass m_1 orbiting inside a parent halo of mass M, the timescale for orbital decay due to dynamical friction is (Binney & Tremaine 2011)

$$t_{\rm df} \approx t_{\rm orb}\left(\frac{M}{m_1}\right)\left(\ln\frac{M}{m_1}\right)^{-1}, \quad (16)$$

After a few $t_{\rm df}$, the subhalo can spiral into the very inner part of the parent halo where they are destroyed by the tidal force of the dense central mass concentration.

Equation (16) suggests that this mechanism is effective on minihalos if the parent halo is a larger minihalo so that M/m_1 is not too large. The orbital timescale is evaluated in Equation (41). For example, a minihalo with $m_1 = 10^{-8}\,M_\odot\,h^{-1}$ can sink to the center of a parent minihalo with $M = 10^{-6}\,M_\odot\,h^{-1}$ within $\sim$3 Gyr. Precise understanding of this hierarchical assembly and destruction of minihalos from white-noise initial density fluctuations will require a dedicated study that employs numerical simulations.

However, many minihalos should evade dynamic friction constraints. First, the PS analysis in Section 4 has shown that a significant fraction of minihalos can be directly bound into either the cluster halo or its galactic-scale subhalos without first being assembled into a moderately larger parent halo or a series of slightly larger parent halos. For these minihalos, the humongous M/m_1 ratio ensures immunity to dynamic friction.

Second, even if a minihalo is first bound into a moderately larger parent halo and starts to spiral in, the parent may be subsequently disrupted by an even larger halo. In this case, the increased M/m_1 ratio allows the minihalo to survive for a longer time. This is especially relevant if the first parent halo is one on the portion of the colored curve in Figure 2 that levels off. In this case, this halo is very susceptible to disruption because subsequent hierarchical mergers take place quickly and involve small density differences. If the original minihalo is quickly "liberated" into orbiting a very large and low-density parent halo, then $t_{\rm df}$ becomes certainly too long compared to the age of the universe.

A subhalo can be destroyed even without spiraling in, simply by being randomly placed into a highly radial orbit toward the very inner part of a larger halo. This can lead to a high-speed encounter with either the central DM density cusp, or possibly with other highly condensed form of matter and compact objects. We will see in the following subsections that these fine-tuned encounters are not the most important processes compared to encounters with other minihalos and ordinary stars.

6.2. High-speed Encounters with Other Subhalos

The large optical depth calculated for Equation (15) of Section 5 and the fact that over the cluster's age minihalos should have completed many orbits inside the cluster halo imply that direct encounters between minihalos are frequent.

We now consider the dynamical heating experienced by a subhalo of mass m_1 and internal velocity dispersion σ_1, when passing close to or moving through another subhalo of mass m_2, due to a random encounter. We focus on high-speed encounters for which the typical encounter relativity velocity[5] σ is much greater than other velocity scales (Aguilar & White 1985; Binney & Tremaine 2011).

We first consider the case $m_2 \simeq m_1$. Then, when the two subhalos fly through each other at an impact parameter b smaller than the subhalo scale radii r_1, the velocity perturbation induced on any particle of the subhalos is $\Delta v \simeq \sigma_1^2/\sigma$, which is a small fraction of σ_1. This is because the tidal perturbation during the encounter is comparable to the orbital acceleration within one halo, but the duration of the encounter is shorter than the orbital time by a factor σ_1/σ. The fractional amount by which the internal subhalo energy varies owing to dynamical heating at each encounter with $b < r_1$ is therefore

$$\frac{\Delta E_1}{E_1} \sim \frac{\sigma_1^2}{\sigma^2}. \quad (17)$$

Dynamical heating scales as the second power of $\Delta v/\sigma_1$ if $\Delta v/\sigma_1 \ll 1$. At the level of individual bound particles of halo m_1, the leading-order fractional change in the particle's energy is linearly proportional to $\Delta v/\sigma_1$, but can be either positive or negative depending on the orbital phase during the encounter. After the halo relaxes back to equilibrium, the average energy injection scales as $(\Delta v/\sigma_1)^2$.

For unequal encounters, the minimum impact parameter is the larger r_s of the two halos. Larger impact parameters are less important, because the induced velocity perturbations scale as b^{-2}, and the internal dynamical heating as b^{-4}, whereas the rate of encounters within b increases only as b^2.

In the case $m_1 < m_2$, an impact parameter b smaller than the scale radius r_2 of the perturber halo m_2 leads to an encounter with the inner density cusp. For an NFW slope of the halo inner density profile, the cusp mass scales as b^2. The velocity perturbation Δv is therefore comparable to that if $b \simeq r_2$, but the probability for a smaller impact parameter is suppressed as $\propto b^2$. This implies that inner density cusps are not the dominant sources of dynamic heating, and it is justified to take the larger r_s of the two halos to be the minimum impact parameter.

At the minimum impact parameter, the induced velocity perturbation is maximized for $m_2 \simeq m_1$. Encounters with a less massive perturber, with $m_2 < m_1$, has $\Delta v \propto m_2$. For encounters with a higher mass halo with $m_2 > m_1$, we focus on minihalos that collapse at high redshifts from the white-noise isocurvature density fluctuations, for which the scale radius goes as $r_2 \propto m_2^{5/6}$. In this case, the tidal acceleration scales as $m_2\, r_2^{-3} \propto m_2^{-3/2}$, and the encounter time as r_2, so $\Delta v \propto m_2^{-2/3}$. As even in the worst case $m_2 \simeq m_1$ we have $\Delta v/\sigma_1 \ll 1$, particle ejections by a single tidal shock are unlikely, and hence the quadratic scaling Equation (17) is justified.

We now show that the cumulative heating from many encounters is still dominated by nearly equal encounters with $m_2 \simeq m_1$. For the case $m_2 < m_1$, dynamical heating per encounter scales as m_2^2, while the encounter rate will scale as $m_2^{-1}\, df_{\rm sub}(m_2; M)/d\ln m_2$. If the PS mass function Equation (9) is applicable to subhalos, $df_{\rm sub}(m_2; M)/d\ln m_2 \propto m_2^{1/2}$ for

[5] Our chosen notation σ is motivated because the typical encounter velocity is set by the internal velocity dispersion of the host halo. This should not be confused with the peak height $\sigma(M, t)$ of the PS formalism.

minihalos, and the encounter rate goes as $m_2^{-1/2}$. In principle, subhalos of subhalos or multiple levels of subhalos also contribute to the disrupting tidal field, which are not included in Equation (9). Without a detailed calculation, we argue that including those $df_{\rm sub}(m_2; M)/d\ \ln m_2$ should depend logarithmically on m_2 because minihalos are not easy to disrupt through hierarchical merging, and accordingly, the encounter rate goes as m_2^{-1}. In either case, the increase in the encounter rate does not compensate for the decreased heating per encounter. For the case $m_2 > m_1$, dynamical heating per encounter decreases as $m_2^{-4/3}$, but the encounter rate increases only as $r_2^2\ m_2^{-1}\ df_{\rm sub}/d\ \ln m_2 \propto m_2^{2/3}\ df_{\rm sub}/d\ \ln m_2$, again insufficient to compensate for the decreased heating per encounter. The above analysis should be valid unless the more massive minihalos have somehow increased their density by dissipative processes above the value reached through virialization at the collapse epoch.

Encounters between halos of comparable masses with impact parameters comparable to their common-scale radii have a rate inside the cluster halo,

$$\Gamma_{\rm enc}(m_1; M) \sim \frac{1}{m_1}\frac{df_{\rm sub}(m_1; M)}{d\ \ln m_1}\frac{R}{t_{\rm orb}(M)}\frac{r_1^2\ M}{R^3}\ , \tag{18}$$

where R is the scale radius of the cluster halo. Given the fractional heating per encounter, Equation (17), the timescale of dynamic disruption is

$$t_{\rm dispt}(m_1; M) \sim t_{\rm orb}(M)\frac{R}{r_1}\left(\frac{df_{\rm sub}(m_1; M)}{d\ \ln m_1}\right)^{-1}, \tag{19}$$

where we have assumed virial equilibrium for both the minihalo and the host halo $R/r_1 = (M/m_1)(\sigma_1/\sigma)^2$. This result can also be expressed in terms of $t_{\rm df}$ of Equation (16),

$$t_{\rm dispt}(m_1; M) \sim t_{\rm df}(m_1; M)\left(\frac{\sigma_1}{\sigma}\right)^2\left(\frac{df_{\rm sub}(m_1; M)}{d\ \ln m_1}\right)^{-1}\ln\frac{M}{m_1}. \tag{20}$$

As the velocity dispersion for minihalos is much smaller than that of the host halo (see Equation (40)), we have $t_{\rm dispt} < t_{\rm df}$. The dominant process for minihalo destruction is therefore dynamical heating by high-speed encounters among comparable minihalos, where they repetitively go through each other before they are disrupted by gradual heating and expansion. Numerically, the disruption timescale is (where we have inserted the relation $G\,M/R \sim \sigma^2$ for the host halo by the virial theorem)

$$\begin{aligned} t_{\rm dispt} \approx\ & 2\times 10^8\ {\rm Gyr}\left(\frac{df_{\rm sub}(m_1; M)}{d\ \ln m_1}\right)^{-1} \\ & \times\left(\frac{M}{10^{15}\,M_\odot\,h^{-1}}\right)^2\left(\frac{\sigma}{10^3\ {\rm km\ s^{-1}}}\right)^{-5} \\ & \times\frac{\nu}{\nu_{\rm med}}\left(\frac{\Omega_a}{0.3}\right)^{1/3}\left(\frac{1+z_{\rm eq}}{3400}\right) \\ & \times\left(\frac{M_0}{10^{-10}\,M_\odot\,h^{-1}}\right)^{1/2}\left(\frac{m_1}{10^{-6}\,M_\odot\,h^{-1}}\right)^{-5/6}. \end{aligned} \tag{21}$$

Even for the largest possible $df_{\rm sub}(m_1; M)/d\ \ln m_1$, this is much longer than the age of the universe within cluster-size or galaxy-size hosts, and even true for minihalos orbiting small CDM halos that form from the adiabatic density fluctuations, say one with $M = 10^6\,M_\odot\,h^{-1}$ and $\sigma = 5\,{\rm km\,s^{-1}}$.

6.3. High-speed Encounters with Stars

After the gas in halos condenses into stars and other compact objects, the potential for the tidal disruption of minihalos is greatly enhanced. The reason for perturber minihalos of similar masses ($m_2 \simeq m_1$) dominating the destruction rate by high-speed encounters rather than perturber minihalos of larger masses has to do with the fact that the more massive minihalos are also less dense, with $\rho_s \propto m_1^{-3/2}$ in the regime that minihalos collapse and assemble from the white-noise initial isocurvature density fluctuations. By contrast, for a compact perturber m_2, the minimum impact parameter is fixed by the size of the minihalo m_1, then the amount of dynamical heating per encounter increases with the mass of the perturbing object as m_2^2. If the number density of perturbers only decreases approximately as m_2^{-1}, dynamical heating should be dominated by the most massive perturbers.

Tidal interactions between generic small halos and passing stars have been extensively studied (Angus & Zhao 2007; Goerdt et al. 2007; Green & Goodwin 2007; Zhao et al. 2007). Here we present a simple order-of-magnitude estimate applied to axion minihalos. A minihalo of mass m_1 and radius r_1 encountering a star with mass $m_\star$ at an impact parameter b and a relative velocity on the order of the host halo's internal velocity dispersion σ is subject to a tidal acceleration $\sim G\,m_\star r_1/b^3$ during the encounter time $\sim b/\sigma$, and suffers an impulsive velocity perturbation,

$$\frac{\Delta v}{\sigma_1} \simeq \frac{G\,m_\star\,r_1}{b^2\,\sigma\,\sigma_1}. \tag{22}$$

Unlike mutual encounters between minihalos, the velocity perturbation induced by a stellar perturber can be large enough that minihalo particles are unbound after a single encounter. This happens for $\Delta v/\sigma_1 \simeq 1$, which sets a minimum impact parameter $b_{\rm min}$ for the minihalo to survive a complete disruption (Goerdt et al. 2007; Schneider et al. 2010; Tinyakov et al. 2016),

$$\begin{aligned} \frac{b_{\rm min}}{r_1} \simeq & \left(\frac{G\,m_\star}{\sigma^2\,r_1}\frac{m_\star}{m_1}\right)^{1/4} \approx 0.7\left(\frac{m_\star}{M_\odot}\right)^{1/2}\left(\frac{\sigma}{10^3\ {\rm km\ s^{-1}}}\right)^{-1/2} \\ & \times\left(\frac{\nu}{\nu_{\rm med}}\right)^{1/4}\left(\frac{\Omega_a}{0.3}\right)^{1/12}\left(\frac{1+z_{\rm eq}}{3400}\right)^{1/4} \\ & \times\left(\frac{M_0}{10^{-10}\,M_\odot\,h^{-1}}\right)^{1/8}\left(\frac{m_1}{10^{-6}\,M_\odot\,h^{-1}}\right)^{-11/24}. \end{aligned} \tag{23}$$

For a range of minihalo parameters, $b_{\rm min}$ is comparable to or larger than the minihalo scale radius r_1. Provided that the overall tidal disruption rate is dominated by encounters with small impact parameters, we therefore conclude that a minihalo is disrupted whenever it passes within $b_{\rm min}$ from a perturber star.

Let $\bar{n}_\star$ be the mean stellar number density within the host halo (including the stellar populations in all member galaxies). The stellar disruption timescale for minihalos orbiting within

the host halo can be estimated as

$$t_{\rm dispt,\star} \sim (\pi\, b_{\rm min}^2\, \bar{n}_\star\, \sigma)^{-1} = \frac{m_1^{1/2}}{\pi\, r_1^{3/2}\, G^{1/2}\, m_\star\, \bar{n}_\star} \approx 50\ {\rm Gyr} \times \left(\frac{m_\star}{M_\odot}\right)^{-1} \left(\frac{\bar{n}_\star}{10^5\ {\rm kpc}^{-3}}\right)^{-1} \times \left(\frac{\nu}{\nu_{\rm med}}\right)^{3/2} \left(\frac{\Omega_a}{0.3}\right)^{1/2} \left(\frac{1+z_{\rm eq}}{3400}\right)^{3/2} \times \left(\frac{M_0}{10^{-10}\, M_\odot\, h^{-1}}\right)^{3/4} \left(\frac{m_1}{10^{-6}\, M_\odot\, h^{-1}}\right)^{-3/4}. \quad (24)$$

Here, the fiducial value $\bar{n}_\star = 10^5\ {\rm kpc}^{-3}$ roughly corresponds to enclosing $\sim 10^{13}\, M_\odot$ of stars within a sphere of $\sim$300 kpc. Note that the internal velocity dispersion of the host halo σ cancels out in this calculation. Equation (24) suggests that the most massive minihalos are the most vulnerable because they are the puffiest. For minihalos in the most interesting mass range concerning this work, $m_1 < 10^{-6}\, h^{-1} M_\odot$, and in axion cosmology scenarios with $M_0 > 10^{-10}\, M_\odot\, h^{-1}$, stellar disruption is not significant throughout the current age of the universe. More massive minihalos, however, are expected to have been destroyed by passing stars in an intracluster environment.

By chance, minihalos can pass the central regions of larger halos at high speed on radial orbits. Apart from stars, supermassive black holes residing at the center of member galaxies are probably the most disruptive perturbers, for which the previous analysis remains applicable. Equation (24) implies that the disruption timescale is inversely proportional to the average mass density of the perturbers within the cluster halo. Despite being much more destructive individually, supermassive black holes still make a smaller contribution to the total mass budget than the stars and hence are not the major sources of disruption.

Finally, we note that even if all minihalos orbiting within the intracluster space are dynamically destroyed, we still expect a remaining contribution from an intergalactic population of minihalos. Those minihalos are not subject to dynamic disruption from encounters with stars. Some of those are isolated, while others are bound to larger intergalactic halos. The latter are susceptible to additional dynamic disruption from mutual encounters inside the parent halo.

7. Impact on Microlensing Lightcurves of Highly Magnified Stars

Despite several theoretical uncertainties, our analyses in the previous sections lead us to the following physical picture if a Peccei–Quinn phase transition in the early universe induces isocurvature density fluctuations on small scales:

1. Minihalos below the mass scale of planets form by gravitational instability starting at the epoch of radiation–matter equality, with characteristic densities much higher than in the standard CDM cosmology.
2. Plenty of these minihalos should survive over the age of the universe as subhalos orbiting inside the halos of galaxy clusters.
3. The high area covering factor of minihalos implies that a line of sight traversing a cluster lens near a typical lensing critical curve (with an impact parameter of tens of kiloparsecs) probes nearly Gaussian random fluctuations in the lensing convergence κ (and hence also in the shear). For the mass scale parameter $M_0 \sim 10^{-13}$–$10^{-6}\, M_\odot h^{-1}$, which corresponds to the first gravitationally collapsed minihalos having masses $\sim 10^{-15}$–$10^{-8}\, M_\odot\, h^{-1}$, the level of fluctuations is $\Delta\kappa \gtrsim 10^{-4}$–$10^{-3}$, on scales of $\sim$10–10^4 au h^{-1}.

In most applications of gravitational lensing, convergence fluctuations of $\sim 10^{-4}$–10^{-3} on the lens plane are too small to lead to any interesting observational consequences. However, caustic transiting stars behind a galaxy cluster lens provide extreme situations in which these minuscule small-scale fluctuations in the convergence can leave observable imprints.

7.1. Detectable Scales of Surface Density Fluctuations under Microlensing

We consider the effect of convergence and shear irregularities on the total flux of a point source. The flux magnification of one image equals the inverse determinant of the lensing Jacobian matrix at the image position, whose matrix elements are expressed in terms of the convergence and shear. When an image is highly magnified ($|\mu| \gg 1$), the corresponding Jacobian matrix is fine-tuned to a level $\sim 1/|\mu|$ to be nearly degenerate. Any irregularity in the convergence and/or shear at a level $\sim 1/|\mu|$ substantially perturbs the image flux.

The detected highly magnified stars behind MACS J1149 (Kelly et al. 2018) and behind MACS J0416 (Chen et al. 2019; Kaurov et al. 2019) are observed thanks to magnification factors of hundreds to thousands. If the projected mass distribution in the cluster lens were smooth, the magnification would simply vary as the inverse of the angular separation from the image to the critical curve, and could reach values above a million when a luminous star crosses the cluster caustic. However, intracluster stars introduce intermittent microlensing flux variations and microcaustic crossings at which a pair of microimages dominate the flux. This makes the highly magnified stars more easily identifiable from their variability, even though the maximum magnifications reached are reduced to $\sim 10^4$ (Venumadhav et al. 2017; Diego et al. 2018; Oguri et al. 2018). Flux variations of up to a factor of 10 have been observed from microlensing events in the fields of MACS J1149 (Kelly et al. 2018) and of MACS J0416 (Chen et al. 2019). During microcaustic crossings, with typical durations of days to weeks, the star flux becomes susceptible to even a minuscule nonsmoothness of $\Delta\kappa \sim 10^{-4}$ in the lens surface density.

During a microcaustic transit event, the two dominant microimages are highly elongated to a length $\approx$5000 au$(|\mu|/10^4)(R_\star/100\, R_\odot)$. Surface density irregularities are detectable down to these scales, which are interestingly comparable to the axion minihalo sizes we have discussed.

7.2. Microfold Model

We now demonstrate how minuscule surface density fluctuations imprint irregularities on microlensing lightcurves. Appendix E shows that geometric optics is applicable to our problem.

For a concrete case study, we consider the highly magnified star LS1 detected in a lensed galaxy at $z_S = 1.49$ behind the cluster lens MACS J1149 at $z_L = 0.544$ (Kelly et al. 2018). This sets the angular diameter distances to the source $D_S = 1.79$ Gpc, to the lens $D_L = 1.35$ Gpc, and from the lens to the source $D_{LS} = 0.95$ Gpc. Two resolved macroimages of LS1 are observed at a separation of $0\farcs13$ from the cluster critical curve, symmetrically positioned around a point where the macrolens model GLAFIC (Kawamata et al. 2016) predicts a surface mass density corresponding to a convergence $\kappa_0 = 0.83$, and a magnification for each macroimage of ∼300.

The presence of microlenses implies that each macroimage actually consists of several unresolved microimages. During a transit of a fold caustic (the most common caustic type), a pair of microimages usually becomes much brighter than the combined flux from all the rest (which is in any case nearly constant). This justifies considering only the two dominant microimages; instead of simulating a network of microlensing caustics induced by many intracluster stars, constructing a simple fold model for the microcaustic crossing suffices. The fold model is described by two parameters: the local convergence $\tilde{\kappa}_0$ and an eigenvalue gradient vector $\tilde{\boldsymbol{d}}$ at the point between the two images along the microcritical curve. The total smooth convergence κ_0 is split into a smooth contribution $\tilde{\kappa}_0$, including the DM and any diffuse baryonic component, and the average contribution from stellar objects, which is $\kappa_\star \approx 0.005$ near the LS1 images in MACS J1149 (Oguri et al. 2018). We use $\tilde{\kappa}_0 = \kappa_0 - \kappa_\star \simeq 0.83$ as a good approximation.

The vector $\tilde{\boldsymbol{d}}$ is perpendicular to the microcaustic and, in the fold approximation, is related to the peak magnification $\mu_{\rm pk}$ at the time when the source stellar disk grazes the microcaustic on the source plane:

$$\mu_{\rm pk} = \frac{1}{2\,|1-\tilde{\kappa}_0|}\left(\frac{D_S}{|\tilde{\boldsymbol{d}}|\,|\sin\tilde{\alpha}|\,R_S}\right)^{1/2} \approx 4\times10^4\left(\frac{|1-\tilde{\kappa}_0|}{0.17}\right)^{-1}\left(\frac{|\tilde{\boldsymbol{d}}|\,|\sin\tilde{\alpha}|}{100\ \mathrm{arcsec}^{-1}}\right)^{-1/2} \times\left(\frac{R_S}{10\,R_\odot}\right)^{-1/2}\left(\frac{D_S}{1\ \mathrm{Gpc}}\right)^{1/2}, \quad (25)$$

where $\tilde{\alpha}$ is the angle between the microcritical curve and the degenerate direction of the local Jacobian matrix, and the stellar radius is R_S. This fold approximation is accurate when the highly magnified images are much closer to the microcritical curve than the typical angular scale of variation of the vector $\tilde{\boldsymbol{d}}$.

The presence of microlenses generates a region around the macrocritical curve of the cluster lens where the microcritical curves interact and join together, forming a network of width $\sim\kappa_\star|\tilde{\boldsymbol{d}}|^{-1}$ (Venumadhav et al. 2017). Within this network, the scale of variation of $\tilde{\boldsymbol{d}}$ is about the mean separation between microlenses, $\sim\theta_\star/\kappa_\star^{1/2}$, where $\theta_\star$ is the Einstein angular radius of each individual microlens of mass $M_\star$, $\theta_\star = (4GM_\star/D_{\rm eff}c^2)^{1/2}$, with $D_{\rm eff} = D_L D_S/D_{LS}$. At the same time, the typical magnitude of $\tilde{\boldsymbol{d}}$ in the corrugated network is

$$|\tilde{\boldsymbol{d}}| \sim \kappa_\star^{3/2}/\theta_\star \sim 350\ \mathrm{arcsec}^{-1} \times\left(\frac{\kappa_\star}{0.01}\right)^{3/2}\left(\frac{M_\star}{1\,M_\odot}\right)^{1/2}\left(\frac{D_{\rm eff}}{1\ \mathrm{Gpc}}\right)^{-1/2}. \quad (26)$$

To demonstrate typical cases, we shall set in the next subsection $|\tilde{\boldsymbol{d}}| = \kappa_\star^{3/2}/\theta_\star$, with fiducial values for $\kappa_\star$ and $M_\star$ as in the above equation. We shall focus on situations of high magnification, with $\mu_{\rm pk} \gtrsim 10^3$–$10^4$, which requires the lensed star to be close enough to a microcaustic. In fact, the typical average magnification of an image at an angular separation $\theta_\star/\kappa_\star^{1/2}$ from a microcritical curve is $\mu \sim |1-\tilde{\kappa}_0|^{-1}(|\tilde{\boldsymbol{d}}|\,|\sin\tilde{\alpha}|\,\theta_\star\kappa_\star^{-1/2})^{-1/2} \sim |1-\tilde{\kappa}_0|^{-1}\,\kappa_\star^{-1/2} \ll 10^3$–$10^4$, for $\kappa_\star \sim 10^{-2}$. For the high magnification of our interest, the two dominant microimages have a much smaller angular separation than $\theta_\star/\kappa_\star^{1/2}$, justifying our use of a fold model locally.

The timescale of caustic transients depends on an effective source velocity v_t. Roughly, this is the relative transverse velocity between the source star and the lens cluster (defined in Equation (12) of Venumadhav et al. 2017), which is constant. Although intracluster stellar microlenses and DM substructure have random velocities of $\sim$1000 km s^{-1} within the host cluster, their impact is dwarfed by the even larger apparent velocity of the microimages on the image plane owing to the large magnification factor. Therefore, for the numerical simulations in the next subsection, the assumptions of a stationary microfold caustic model and time-independent realizations of axion minihalos along the line of sight are justified.

7.3. Numerical Examples

The analytical estimates in Equation (25) and (26) suggest that microlensing peak magnifications can reach $\sim10^3$–10^4 for reasonable lens and source parameters. We employ a numerical simulation to verify that fractional fluctuations $\sim10^{-4}$–10^{-3} in the lens surface density on appropriate scales are sufficient to imprint observable effects in the total flux.

On top of the microfold model, we add a spatially varying convergence perturbation $\Delta\kappa$ due to minihalos. Without having to generate individual minihalos, we are justified to model $\Delta\kappa$ as a Gaussian random field as shown in Section 5. We generate random realizations of $\Delta\kappa$ according to the homogeneous and isotropic power spectrum in Equation (14), converting the linear Fourier wave vector to the angular Fourier wave vector $\ell = D_L\,\boldsymbol{q}_\perp$. In the case of MACS J1149, the critical surface density is computed to be $\Sigma_{\rm crit} = 2.3\times10^9\,M_\odot\,\mathrm{kpc}^{-2}$ and $\bar{\Sigma}_{\rm cl} = 0.83\,\Sigma_{\rm crit}$. The perturbed deflection required for inverse ray-tracing can then be computed in the Fourier domain $\Delta\boldsymbol{\alpha}(\ell) = (-2\,i\,\ell/\ell^2)\Delta\kappa(\ell)$.

In Figure 6, we present a numerical example of how minihalos collectively induce irregularities in the lightcurve during a microcaustic transit event, assuming parameters appropriate for the case of MACS J1149 LS1. In the absence of minihalos, the total flux rises smoothly as $|t-t_*|^{-1/2}$ after the two highly elongated microimages become dominant, peaks when the finite source effect kicks in, and then plummets when the two microimages merge and disappear.

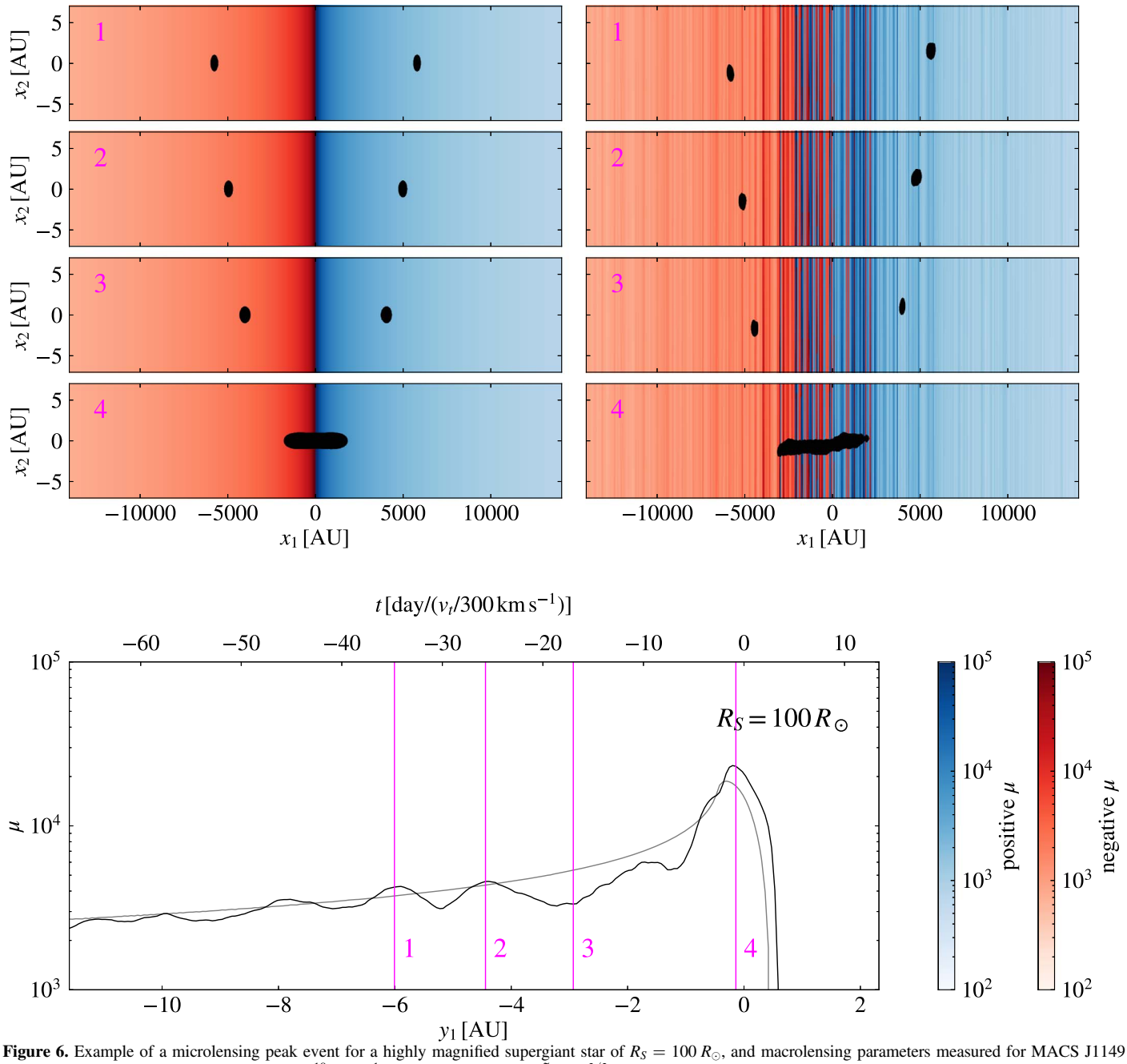

Figure 6. Example of a microlensing peak event for a highly magnified supergiant star of $R_S = 100\,R_\odot$, and macrolensing parameters measured for MACS J1149 LS1. For axion cosmology, we set $M_0 = 10^{-10}\,M_\odot h^{-1}$. We set $\tilde{\alpha} = \pi/2$ and $|\tilde{\boldsymbol{d}}| = \kappa_\star^{3/2}/\theta_\star$, with $\kappa_\star = 0.005$ and $\theta_\star$ computed for a microlens mass $M_\star = 0.3\,M_\odot$. Top four rows: dominant microimage pair in the image plane (in proper length units) and magnification pattern including its sign, with (right column) and without (left column) small-scale surface density fluctuations due to axion minihalos. Coordinates x_1 and x_2 (shown on drastically different scales!) are parallel and perpendicular, respectively, to the degeneracy direction of the local microfold model. Each row corresponds to a numbered epoch. Color scales for magnification are shown to the right of the bottom panel. Bottom row: total flux magnification vs. the source's one-dimensional position y_1 (in proper units) in the source plane and the variability timescale converted from an effective source velocity v_t, with (black curve) and without (gray curve) surface density fluctuations, due to minihalos. The coordinate y_1 measures the position perpendicular to the microcaustic. Only contributions from the two dominant microimages are included. The four numbered epochs examined in the top rows are marked by magenta lines.

Minihalos cause sizable brightening and fading "bumps" in the lightcurve despite the minuscule surface density fluctuations they induce. As the microlensing peak is approached, these irregularities become more prominent. In this example, the irregularities occur on a timescale of several days for $v_t \sim 300\,\mathrm{km\,s^{-1}}$. Unlike the usual microlensing signature of compact lenses, these irregularities lack abrupt changes; due to caustic crossings, microlensing lightcurves usually show asymmetric peaks, which have a slowly varying wing followed by an abrupt cutoff, or the time-reversed behavior.

In the perturbed lightcurve, the time of microimage merger shifts relative to that in the unperturbed one. This is due to coherent deflection perturbation generated by long wavelength modes. Causing merely a uniform remapping of the image plane coordinates, this bears no observable significance.

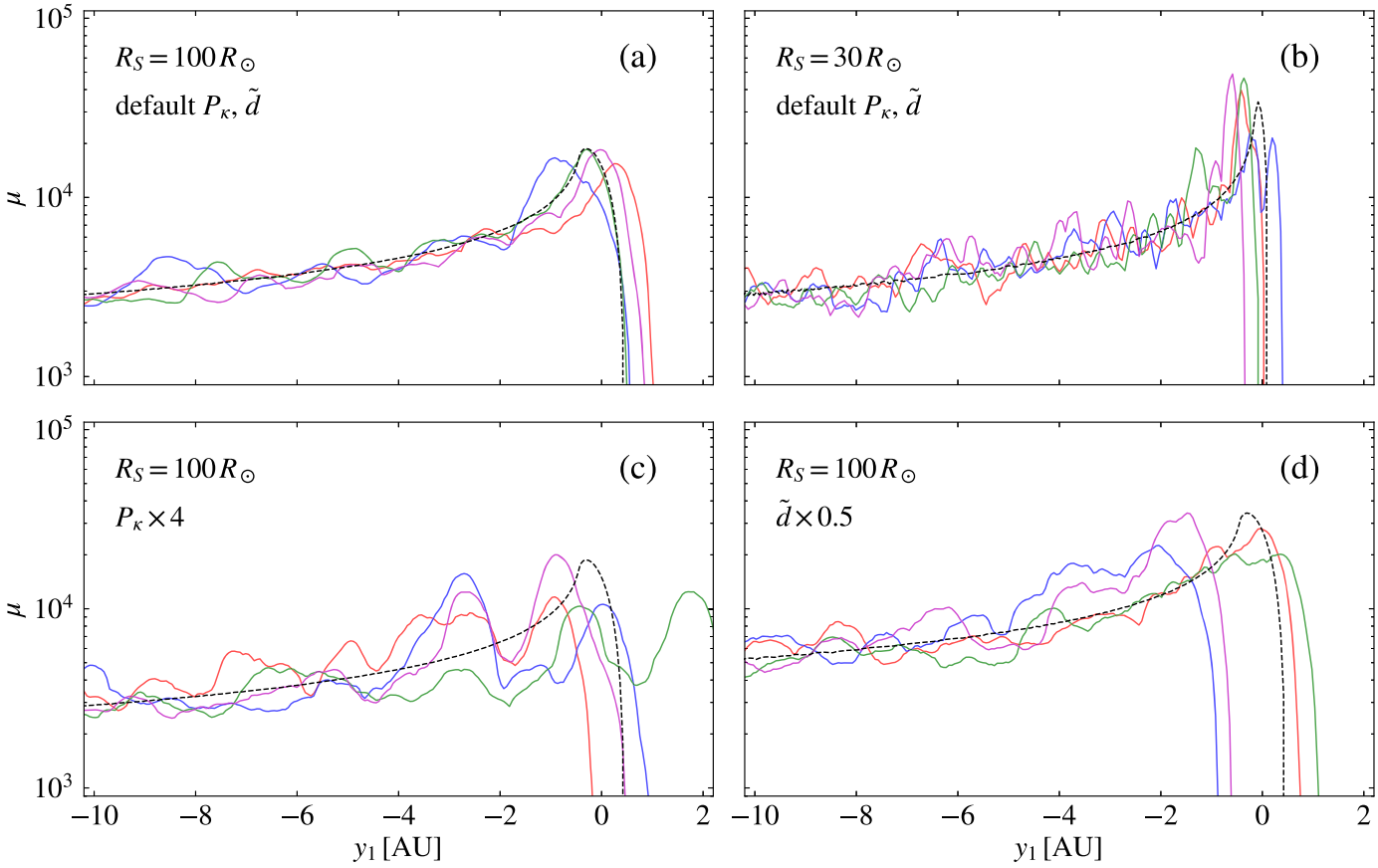

Figure 7. Perturbed lightcurves (colored curves) compared to a smooth lightcurve (dashed black curve) around the time of a microlensing peak event. Each panel shows four random realizations of convergence fluctuations (one color for each). (a) Default case as in Figure 6. (b) A more compact source star with $R_S = 30\,R_\odot$. (c) Power spectrum P_κ enhanced by a factor of 4. (d) $\tilde{d} = |\tilde{\boldsymbol{d}}|$ decreased by a factor of 2.

As visualized in Figure 6, we observe that the perturbing effect is one-dimensional in nature: only nonsmoothness along the degenerate direction of the microfold matters as the two microimages are highly elongated along this direction.

The perturbed lightcurve varies depending on a number of factors, as we show in Figure 7. First, the length of the elongated microimage scales with the source size, which smooths out irregularities below certain scales. For a smaller source star, therefore, irregularities are present on shorter timescales.

Second, larger convergence fluctuations will result in larger magnitude irregularities. This can be the case if more minihalos survive dynamic disruption and are bound to intermediate sized subhalos, as the amount of minihalos contributing to surface density clumpiness will then be more than what Equation (14) predicts.

Moreover, susceptibility to lensing perturbations depends on the $\tilde{\boldsymbol{d}}$ vector of the microfold model. Although in Figure 6 we have set $|\tilde{\boldsymbol{d}}| = \kappa_\star^{3/2}/\theta_\star$, $|\tilde{\boldsymbol{d}}|$ actually varies among microcaustic crossing events. At a fixed distance from the microcaustic, a smaller $|\tilde{\boldsymbol{d}}|$ corresponds to a larger magnification of the two microimages. This means that the flux is more prone to surface density perturbations and is subject to larger irregularities.

If the typical convergence fluctuation $\Delta\kappa$ greatly exceeds the inverse magnification factor, even a microimage can be strongly perturbed and break into yet smaller images. For example, this is likely the case for the scenario with $M_0 = 10^{-6}\,M_\odot\,h^{-1}$ shown in the left panel of Figure 4. The underlying physical principle is analogous to the disruption of macroimages into microimages due to a supercritical number density of intracluster microlenses (Venumadhav et al. 2017; Diego et al. 2018; Oguri et al. 2018), or due to a high abundance of CDM subhalos (Dai et al. 2018b). A detailed analysis of this regime of strong image disruption is beyond the scope of this work but is certainly an important situation to consider. Excessively large surface density fluctuations on length scales being considered here should be constrained by microlensing observations because they would smooth out stellar microlensing peaks.

8. Discussion

Minihalos are predicted to form in many cases when the dark matter is composed of axion particles that can solve the strong CP problem of QCD. So far, no viable method for detecting these axion minihalos through their gravitational lensing effect has been proposed. A generic problem to detect them is their low surface density. This paper proposes that axion minihalos can be detected during extreme magnification events when luminous stars cross microcaustics produced by intracluster stars near the macrocritical curves of massive galaxy clusters. Substantial deviations from the predicted lightcurve of a fold microcaustic crossing over timescales from hours to days will be the signature of large numbers of axion minihalos which should superpose along a line of sight to produce nearly Gaussian fluctuations in the surface density.

The predicted lightcurve will in general be affected by limb-darkening effects in the source star. These effects should nevertheless be accurately predictable once the spectral type of the source star is known. An irregular behavior of the flux might, however, arise for other physical reasons. We now

discuss some of these other possible sources of deviations from a predicted lightcurve.

8.1. Microlensing by Planet-sized Lenses

Planets or planetesimals inside the foreground galaxy cluster may imprint distortions onto stellar microlensing lightcurves. Inside the microcritical curve network, and without substellar lenses, the typical separation between a segment of microcritical curve and nearby microlens stars is $\sim(\kappa_\star\,\Sigma_{\rm crit}/M_\star)^{-1/2}$ $\approx 0.1\ {\rm pc}(\kappa_\star/0.01)^{-1/2}(D_{\rm eff}/1\ {\rm Gpc})^{1/2}(M_\star/0.3\ M_\odot)^{1/2}$. Bound planets orbiting their host stars much more closely than this do not induce independent critical curves.

If any rogue or wide-orbit planets lie far (in projection) from any stellar critical curves, the minimal surface density for them to form a finer network of critical curves is $\kappa_{\rm ffp}\gtrsim 1/\bar{\mu}$, where $\bar{\mu}\sim 100$–1000 is the magnification factor of the image being observed. This would require a comparable amount of mass in rogue planets and stars, which is ruled out by Milky Way microlensing surveys implying $\kappa_{\rm ffp}\lesssim 10^{-3}\,\kappa_\star$ (Sumi et al. 2011; Mróz et al. 2017).

Free-floating planets which happen to lie in the vicinity of the stellar microcritical curve can have greatly enhanced microlensing effects. If these planets have mass $M_{\rm ffp}$, corresponding to an angular Einstein scale $\theta_{\rm ffp}$, one requires $\kappa_{\rm ffp}\gtrsim(\theta_{\rm ffp}\,\tilde{d})^{2/3}\sim\kappa_\star(M_{\rm ffp}/M_\star)^{1/3}$ for breakup of stellar microcritical curves to be common (Venumadhav et al. 2017). This implies a much higher abundance of free-floating planets than main-sequence stars, which is unlikely.

If the stellar microcritical curve is indeed substantially disrupted by substellar lens objects (see, e.g., Dai & Guerras 2018, for an analogous consideration of quasar microlensing), finer variability structures are expected in the lightcurve near a stellar microlensing peak. However, in this case, signatures of planets or planetesimals would likely be sharp minor peaks rather than smoothly behaved irregularities.

8.2. Blended Source Stars

The observed flux of the magnified star within its point-spread function is likely to be contaminated by blended fainter stars. Although lensing of these fainter stars (or intrinsic variability if they are Cepheids) could contaminate the lightcurve, this is unlikely to happen because the highly magnified stars that are observed are usually among the most luminous in a galaxy, and they are sufficiently rare to make the superposition of two detectable lensed stars highly improbable. Contaminating microlensing is expected to produce sharp minor peaks in the lightcurve rather than the more smoothly behaved irregularities from axion minihalos, as can be seen in Figures 6 and 7. If the contaminator is of a different stellar type, variability will be chromatic, which is not generally expected from the lensing of a single star.

8.3. Inhomogeneous Gas

The dominant baryonic component inside a cluster halo is the ionized gas, which is shock heated to $T\sim 10^8$ K and has a number density $n_e\sim 10^{-3}\,{\rm cm}^{-3}$. What is of our concern is the surface density fluctuations in the intracluster gas along the line of sight. However, what matters to the inquiry of this paper is inhomogeneities on minuscule scales $\sim$10–10^4 au, which is orders of magnitude smaller than even the mean free path $\lambda_{\rm mfp}\sim 1$ pc of the dilute gas. Although X-ray surface brightness measurements have clearly shown sizable turbulent density fluctuations $\Delta\delta_{\rm gas,3d}\sim 10\%$ (fractional) on scales of 10–1000 kpc (Schuecker et al. 2004; Kawahara et al. 2008; Churazov et al. 2012), the characteristic amplitude of fluctuation is expected to decrease toward smaller scales following a Kolmogorov-like power law $\Delta\delta_{\rm gas,3d}(k)\propto k^\alpha$ with $\alpha\simeq -1/3$ (Gaspari et al. 2014) and is likely to cut off well before scales of $1/k\sim 10$–10^4 au due to dissipation (Luan & Goldreich 2014). For fixed volumetric density fluctuation, the surface density fluctuation is further suppressed by projection $\Delta\delta_{\rm gas,2d}(q_\perp)\sim\Delta\delta_{\rm gas,3d}(q_\perp)(q_\perp\,L)^{-1/2}$ (Appendix C), where $L\sim 1$ Mpc is the path length traversing the gas halo. Given the huge hierarchy between our projected scale of interest $1/q_\perp$ and L, roughly $q_\perp L\sim 10^7$–10^{10}, we hardly expect any detectable contribution to the lens surface density fluctuations from the hot diffuse gas. Cold and compact ISM gas structures of tiny sizes, if existing, may possibly perturb microlensing lightcurves, although their abundance and physical properties in the intracluster environment or in the surroundings of the BCG are poorly known. The lensing phenomenon we have been considering will probe or constrain any such small-scale baryonic structures.

9. Conclusion

Recently discovered lensed individual stars behind cluster lenses have the largest magnification factors among all currently known gravitational lensing phenomena. Flux amplification by $\sim 10^3$–10^4 is expected when they transit microlensing caustics induced by intracluster stars. We have shown that, during these extreme magnification events, their lightcurves are susceptible to minuscule nonsmoothness $\sim 10^{-3}$–10^{-4} in the lens surface mass density, across very small projected scales $\sim$10–10^4 au, which are hardly accessible with other observational means.

Within the strongly motivated paradigm of axion DM particles, solar system sized minihalos in the mass range $M\sim 10^{-10}$–$10^{-6}\,M_\odot$ are predicted to copiously orbit the DM halo of galaxy clusters. This prediction should be generic if the Peccei–Quinn symmetry breaking occurs after inflation. Our calculations have shown, for a promising range of axion mass, that a large number of minihalos along the line of sight are able to collectively induce detectable surface density fluctuations. This result applies to $M_0=10^{-13}$–$10^{-6}\,M_\odot h^{-1}$, translating into typical masses for the earliest gravitationally collapsed minihalos in the range $\sim 0.01\,M_0\approx 10^{-15}$–$10^{-8}\,M_\odot$, an interval which includes the predicted parameters for the QCD axion. To our knowledge, monitoring microlensing variability of highly magnified stars is the first practical lensing-based method to probe axion minihalos.

Primordial black holes formed in the early universe are another DM candidate (Zel'dovich & Novikov 1967; Hawking 1971; Carr & Hawking 1974; Carr et al. 2016; García-Bellido 2017). The mass budget of stellar-mass black holes (Bird et al. 2016; Sasaki et al. 2016; Clesse & García-Bellido 2017) has been subject to stringent limits set by microlensing and dynamics. Recently, however, Montero-Camacho et al. (2019) showed that the majority of DM may be made of black holes in the mass range $10^{-17}\,M_\odot\lesssim M_{\rm PBH}\lesssim 10^{-12}\,M_\odot$ without contradicting known astrophysical constraints. Such primordial black holes of asteroid masses may cluster into minihalos in a hierarchical fashion (see, e.g., Inman & Ali-Haïmoud 2019), created from a white-noise power spectrum in a similar way as

axion minihalos, and they may produce similar lensing effects as the axion minihalos although with some detailed differences arising from dynamical relaxation and the discrete nature of black holes that may give rise to distinct observational signatures.

Accurate and high-cadence lightcurves of highly magnified stars around the times of microlensing caustic transits have not been acquired so far. This will require dedicated monitoring using either space telescopes or large ground-based telescopes to reach the extremely faint fluxes at optical or near-infrared wavelengths, executed over days to weeks around the peak time with high cadence. In the case of stars lensed by MACS J1149 and MACS J0416, one or two microlensing peaks were mapped out only at crude levels. Since microlensing caustic transits occur randomly, an approximate time window bracketing the moment of flux culmination will need to be forecasted based on low-cadence premonitoring that can detect a trend in which the star gradually brightens following a $f_\nu \propto |t - t_0|^{-1/2}$ law. Because any detected highly magnified star is generally expected to undergo intermittent microcaustic transits for many years to follow, and the opportunity to discover DM minihalos or any other dark or baryonic small-scale lumpiness is unique and highly rewarding, there is a strong incentive to design and carry out these programs.

The authors would like to thank Scott Tremaine and Matias Zaldarriaga for insightful discussions, and Ken Van Tilburg for helping us clarify issues regarding the expected mass scale of QCD axion minihalos. We acknowledge the use of the publicly available Python package `Colossus` to carry out cosmological calculations (Diemer 2018). L.D. acknowledges the support from the Raymond and Beverly Sackler Foundation Fund. J.M. has been partly supported by Spanish fellowship PRX18/00444 and by the Corning Glass Works Foundation Fellowship Fund.

Appendix A
Mass Scale of First Gravitationally Collapsed Minihalos

We evaluate the mass parameter M_0 defined in Equation (1) for the standard cosmological thermal history. In this appendix, we adopt the natural units for which $c = \hbar = k_B = 1$.

Let T_0 be the radiation temperature at time t_0 at the onset of axion field oscillation. The axion mean density at present is $\bar{\rho}_{a0} = (3\,H_0^2\,\Omega_a)/(8\,\pi\,G)$. In Equation (1), we write $k_0 = a(t_0)H(t_0)$. The scale factor at t_0 is

$$a(t_0) = \left(\frac{T_{\gamma 0}}{T_0}\right)\left[\left(2 + 6\,\frac{7}{8}\left(\frac{T_{\nu 0}}{T_{\gamma 0}}\right)^3\right)\frac{1}{g_{*s}}\right]^{1/3}, \tag{27}$$

where the temperature of the CMB $T_{\gamma 0} = 2.725$ K, the temperature of the relic neutrinos $T_{\nu\,0} = (4/11)^{1/3}\,T_{\gamma\,0}$, and $g_{*s} \approx 78$ is the effective number of relativistic degrees of freedom for entropy when the temperature is $\sim$1 GeV (Husdal 2016). We calculate the Hubble parameter $H(t_0)$ using the Friedmann equation during the era of radiation domination $H(t_0) = [(8\,\pi\,G/3)(\pi^2/30)g_{*\epsilon}\,T_0^4]^{1/2}$, where $g_{*\epsilon} \approx 78$ is the effective number of relativistic degrees of freedom for energy density at a temperature $\sim$1 GeV (Husdal 2016). Putting all the pieces together, we find

$$M_0 = 10^{-9}\,M_\odot\,h^2\left(\frac{\Omega_a}{0.27}\right)\left(\frac{T_0}{1.3\ \mathrm{GeV}}\right)^{-3}\left(\frac{g_{*s}}{78}\right)\left(\frac{g_{*\epsilon}}{78}\right)^{-3/2}. \tag{28}$$

We note that our definition of M_0 is adopted from Fairbairn et al. (2018), which is a factor of $4\pi^4/3$ larger than what is used in several other references (e.g., Davidson & Schwetz 2016; Hardy 2017). Following the definition of the latter authors, the typical mass for the smallest minihalos that collapse the earliest from gravitational instability should be two orders of magnitude smaller than M_0. The exact number is not sharply defined because even these minihalos contain finer axion substructures as uncovered in numerical simulations.

Appendix B
Linear Growth of Isocurvature Modes

Under the assumption that the DM is made of axions, the isocurvature matter modes under consideration here are superhorizon modes at the onset of axion field oscillation, but enter the horizon during the era of radiation domination. These perturbations do not grow during the radiation-dominated epoch. After the epoch of radiation–matter equality, they lock onto a growing mode that scales linearly with the scale factor.

To verify this picture, consider a toy universe composed of a radiation fluid and a matter fluid that does not interact with the radiation. We normalize the scale factor such that it is equal to unity $a_\star = 1$ when the mean radiation density equals the mean matter density $\rho_r(a_\star) = \rho_m(a_\star)$. Define a synchronous-comoving coordinate system in which the peculiar velocity of the matter fluid is always zero. We can derive the following set of equations (Efstathiou & Bond 1986; Ma & Bertschinger 1995)

$$h'' + \frac{2 + 3\,a}{2\,a(1 + a)}\,h' = \frac{3}{a^2(1 + a)}(2\,\delta_r + a\,\delta_m), \tag{29}$$

$$\delta_m' = \frac{1}{2}\,h', \tag{30}$$

$$\delta_r' = \frac{2}{3}\,h' - \frac{4}{3}\,\chi_r, \tag{31}$$

$$\chi_r' = \frac{\chi_r}{2\,a(1 + a)} + \left(\frac{c\,k}{a_\star\,H_\star}\right)\frac{\delta_r}{2(1 + a)}. \tag{32}$$

Here, $a_\star$ and $H_\star = H(a_\star)$ are the scale factor and the Hubble parameter at the epoch of radiation–matter equality, respectively, δ_m and δ_r are matter and radiation overdensities, respectively, h is the trace of the spatial metric perturbation in the synchronous gauge (to be distinguished from the dimensionless Hubble parameter h elsewhere), and we have defined $\chi_r \coloneqq \theta_r/(a^2\,H)$ with θ_r being the velocity divergence of the radiation fluid. The notation $(\cdots)'$ represents the derivative with respect to the scale factor a.

We consider modes that enter the horizon well before the epoch of radiation–matter equality $c\,k/(a_\star\,H_\star) \gg 1$. The isocurvature initial condition is set at some initial time a_i in the superhorizon regime $ck/(a_iH(a_i)) \ll 1$. At the initial time, the isocurvature initial condition requires $\delta_r(a_i) = -\,\delta_m(a_i)a_i$, $\chi_r(a_i) = h(a_i) = h'(a_i) = 0$.

In the limit of matter domination $a \to \infty$, the matter mode satisfies

$$\delta_m'' + \frac{3}{2\,a}\,\delta_m' - \frac{3}{2\,a^2}\,\delta_m = 0, \tag{33}$$

which has a growing solution $\delta_m \propto a$.

By numerically solving the above set of linear equations, we find that deep in the era of matter domination $a \gg 1$, the solution for the matter perturbation is roughly

$$\delta_m(a) = C\,\frac{a}{a_\star}\,\delta_m(a_i), \tag{34}$$

where C is an order-unity coefficient with a logarithmic dependence on $ck/(a_\star H_\star)$. The exact value of C is cosmology dependent, but its value is not much different from unity.

We note that in principle the initial isocurvature overdensity can be much greater than unity. In this case, virialized structures can form well before the epoch of radiation–matter equality (Kolb & Tkachev 1994; Enander et al. 2017). A distribution of large initial overdensity patches were suggested by Kolb & Tkachev (1996) according to numerical results. Microlensing constraints, e.g., suggested by Fairbairn et al. (2017, 2018), have relied on ruling out extremely compact mini structures that collapse from such patches. We caution that it is unclear whether an extrapolation to huge initial overdensity values is physically plausible in realistic models, or whether such patches are sufficiently common to be important. This study restricts to initial isocurvature fluctuations not much greater than unity.

Appendix C
Surface Density Power Spectrum

In this appendix, we consider a slab with a homogeneous and isotropic clumpiness property. We derive the relation between the two-dimensional power spectrum of the surface density field and the three-dimensional power spectrum of the volumetric density field.

We focus in the regime where the slab length L along the direction of projection (i.e., the line of sight) is much larger than the dimensions perpendicular to the direction of projection (i.e., parallel to the plane of the sky). The surface density field can be written as

$$\Sigma(\boldsymbol{r}_\perp) = \int_{-L/2}^{L/2} dr_\parallel\,\rho(\boldsymbol{r}) = \int_{-L/2}^{L/2} dr_\parallel \int_{-\infty}^{+\infty} \frac{dq_\parallel}{(2\pi)} \times \int \frac{d^2\boldsymbol{q}_\perp}{(2\pi)^2}\,\tilde{\rho}(\boldsymbol{q}) \exp\left[i(q_\parallel\, r_\parallel + \boldsymbol{q}_\perp \cdot \boldsymbol{r}_\perp)\right]. \tag{35}$$

Here, $r_\parallel$ and $\boldsymbol{r}_\perp$ are the coordinates, in proper units, along and perpendicular to the direction of projection, respectively. The three-dimensional wave vector $\boldsymbol{q}$ can be decomposed into a perpendicular component $\boldsymbol{q}_\perp$ and a parallel component. The Fourier transform of the surface density field is

$$\tilde{\Sigma}(\boldsymbol{q}_\perp) = \int_{-L/2}^{L/2} dr_\parallel \int_{-\infty}^{+\infty} \frac{dq_\parallel}{(2\pi)}\,\tilde{\rho}(\boldsymbol{q})\, e^{i\,q_\parallel\, r_\parallel}. \tag{36}$$

Using $\langle \tilde{\rho}(\boldsymbol{q})\tilde{\rho}^*(\boldsymbol{q}')\rangle = (2\pi)^3\,\delta_D(\boldsymbol{q}-\boldsymbol{q}')P_\rho(q)$, we can calculate

$$\begin{aligned}\langle \tilde{\Sigma}(\boldsymbol{q}_\perp)\tilde{\Sigma}^*(\boldsymbol{q}_\perp')\rangle &= \int_{-L/2}^{L/2} dr_\parallel \int_{-L/2}^{L/2} dr_\parallel' \\ &\quad\times \int_{-\infty}^{+\infty} \frac{dq_\parallel}{(2\pi)} \int_{-\infty}^{+\infty} \frac{dq_\parallel'}{(2\pi)} \\ &\quad\times (2\pi)^3\,\delta_D(\boldsymbol{q}_\perp - \boldsymbol{q}_\perp')\delta_D(q_\parallel - q_\parallel') \\ &\quad\times P_\rho\left(\sqrt{q_\parallel^2 + \boldsymbol{q}_\perp^2}\right) e^{i(q_\parallel r_\parallel - q_\parallel' r_\parallel')} \\ &= (2\pi)^2\,\delta_D(\boldsymbol{q}_\perp - \boldsymbol{q}_\perp') \int_{-L/2}^{L/2} dr_\parallel \int_{-L/2}^{L/2} dr_\parallel' \\ &\quad\times \int_{-\infty}^{+\infty} \frac{dq_\parallel}{(2\pi)}\, P_\rho\left(\sqrt{q_\parallel^2 + \boldsymbol{q}_\perp^2}\right) e^{iq_\parallel(r_\parallel - r_\parallel')} \\ &= (2\pi)^2\,\delta_D(\boldsymbol{q}_\perp - \boldsymbol{q}_\perp') \int_{-\infty}^{+\infty} \frac{dq_\parallel}{(2\pi)} \\ &\quad\times P_\rho\left(\sqrt{q_\parallel^2 + \boldsymbol{q}_\perp^2}\right)\left[\frac{2\sin(q_\parallel L/2)}{q_\parallel}\right]^2.\end{aligned} \tag{37}$$

Therefore, the projected power spectrum is

$$P_\Sigma(q_\perp) = \int_{-\infty}^{+\infty} \frac{dq_\parallel}{(2\pi)}\, P_\rho\left(\sqrt{q_\parallel^2 + q_\perp^2}\right)\left[\frac{2\sin(q_\parallel L/2)}{q_\parallel}\right]^2. \tag{38}$$

The regime we are interested in is $q_\perp L \gg 1$.

We specialize to the case wherein $P_\rho(q) \propto q^\gamma$ with $\gamma < 1$. In this case, the dominant contribution to the integral comes from modes with $q_\parallel \ll q_\perp$ but $q_\parallel \sim 1/L$. We therefore obtain $P_\Sigma(q_\perp) \sim P_\rho(q_\perp)L$. Carrying out the $q_\parallel$ integral explicitly, we can fix the normalization factor of order unity and obtain

$$P_\Sigma(q_\perp) = P_\rho(q_\perp)L. \tag{39}$$

This relation can be verified for a halo model of density inhomogeneity. Under the assumption that halos are uniformly distributed in space, $P_\rho(q)$ and $P_\Sigma(q)$ can be explicitly computed in terms of the halo mass function and the halo density profiles, and Equation (39) indeed holds.

Appendix D
Dynamic Scales of Minihalos

Minihalos that form from the white-noise isocurvature density fluctuations have extremely small internal velocity dispersions,

$$\begin{aligned}\sigma_v(M) &\sim [G\,\rho_s(M) r_s^2(M)]^{1/2} \\ &\simeq 2\times 10^{-4}\,\mathrm{km\,s^{-1}} \left(\frac{\nu}{\nu_{\rm med}}\right)^{1/2}\left(\frac{\Omega_a}{0.3}\right)^{1/6} \\ &\quad\times \left(\frac{1+z_{\rm eq}}{3400}\right)^{1/2}\left(\frac{M_0}{10^{-10}\,M_\odot\,h^{-1}}\right)^{1/4}\left(\frac{M}{10^{-6}\,M_\odot\,h^{-1}}\right)^{1/12}.\end{aligned} \tag{40}$$

Generally, $\sigma_v(M)$ is much smaller than the internal velocities of large CDM halos of any galaxies or galaxy clusters,

$\sim$1–1000 km s^{-1}. The orbital timescale is

$$t_{\rm orb}(M) \sim \frac{r_s(M)}{\sigma_v(M)} \simeq 30\, h^{-1}\,{\rm Myr}\left(\frac{1+z_{\rm eq}}{3400}\right)^{-3/2}\left(\frac{\nu}{\nu_{\rm med}}\right)^{-3/2}\left(\frac{\Omega_a}{0.3}\right)^{-1/2} \times \left(\frac{M_0}{10^{-10}\,M_\odot\,h^{-1}}\right)^{-3/4}\left(\frac{M}{10^{-6}\,M_\odot\,h^{-1}}\right)^{3/4}. \quad (41)$$

These timescales are much shorter than the age of the present universe but are usually not so short compared to galactic orbital timescales. Even for minihalos of $M = 10^{-10}\,M_\odot h^{-1}$, the dynamic timescale $\sim$30 kyr is quite long.

Inside a galaxy cluster, minihalos are flying around at the huge internal velocities of clusters, $\sigma_{\rm cl} \sim 1000\,{\rm km\,s^{-1}}$, taking less than a few years to cross the size of even the largest axion minihalos under our consideration. Therefore, dynamic interactions among minihalos are always much faster than their internal orbital timescales, which is in the regime of high-speed encounters.

Appendix E
Validity of Geometric Optics

We show here that in the context of lensing discussed in this paper, geometric optics is valid if observations are done at UV, optical, or near-infrared wavelengths. The angular size of a typical star producing the observed microcaustic crossing events regulates the maximum magnification factor, up to a wavelength at which wave diffraction effects become important. Simple estimates are presented in this appendix to justify that.

For a single lens plane, the chromatic amplification factor for the amplitude of an electromagnetic wave is given by the following diffraction integral (see, e.g., Dai et al. 2018a):

$$F(\lambda) = \frac{(1+z_L)}{i\,\lambda}\,\frac{D_L\,D_S}{D_{LS}} \times \int d^2\boldsymbol{x}\,\exp\left[i\,2\pi\,c(1+z_L)\tau(\boldsymbol{x};\boldsymbol{y})/\lambda\right], \quad (42)$$

where λ is the wavelength and $\tau(\boldsymbol{x};\boldsymbol{y})$ is the ray travel time as a function of the source position $\boldsymbol{y}$ and the image position $\boldsymbol{x}$,

$$\tau(\boldsymbol{x};\boldsymbol{y}) = \frac{D_L\,D_S}{c\,D_{LS}}\left[\frac{1}{2}(\boldsymbol{x}-\boldsymbol{y})^2 - \phi(\boldsymbol{x})\right]. \quad (43)$$

Considering only the two dominant microimages during a microcaustic transit, the Shapiro term $\phi(\boldsymbol{x})$ can be written as the sum of the contribution from the microfold model and a stochastic contribution from surface density fluctuations, $\phi(\boldsymbol{x}) = \phi_{\rm fold}(\boldsymbol{x}) + \Delta\phi(\boldsymbol{x})$.

Geometric optics is valid if the diffraction integral in Equation (42) can be replaced by complex Gaussian integrals around extrema of $\tau(\boldsymbol{x};\boldsymbol{y})$. This requires that $\tau(\boldsymbol{x};\boldsymbol{y})$ is locally well approximated by a quadratic function of $\boldsymbol{x}$ in the lowest order Fresnel zones, which in the case of an elongated microimage with magnification μ has angular dimensions

$$\frac{\Delta x_1}{\sqrt{|\mu|}} \sim \Delta x_2 \sim \left[\frac{\lambda}{2\pi(1+z_L)D_0}\right]^{1/2}, \quad (44)$$

where we denote $D_0 = D_L D_S/D_{LS}$. The validity of the quadratic approximation for $\tau(\boldsymbol{x};\boldsymbol{y})$ around extrema is typically limited by the longer dimension Δx_1.

For the microfold model, the third derivative of $\tau(\boldsymbol{x};\boldsymbol{y})$ is typically comparable to $|\tilde{\boldsymbol{d}}|$. So, the departure from the quadratic approximation for the phase of the integrand in Equation (42) is roughly

$$\left[\frac{\lambda}{2\pi(1+z_L)D_0}\right]^{1/2}\sqrt{|\mu|}\;|\tilde{\boldsymbol{d}}| \sim \frac{10^{-6}\,{\rm rad}}{(1+z_L)^{1/2}}\left(\frac{\lambda}{1\,\mu{\rm m}}\right)^{1/2}\left(\frac{D_0}{1\,{\rm Gpc}}\right)^{-1/2} \times \left(\frac{|\mu|}{10^4}\right)^{1/2}\left(\frac{|\tilde{\boldsymbol{d}}|}{10^3\,{\rm arcsec^{-1}}}\right). \quad (45)$$

This is negligibly small for reasonable parameters considered in this paper.

If included, small-scale surface density fluctuations may be the dominant contribution to the third derivative of $\tau(\boldsymbol{x};\boldsymbol{y})$. The characteristic amplitude can be estimated as $\sim\Delta_\kappa/(r_\perp/D_L)$, where the convergence fluctuation has a typical amplitude Δ_κ on a typical transverse proper length scale $r_\perp$. Similar to Equation (45), the correction to the phase of the diffraction integrand is

$$\left[\frac{\lambda}{2\pi(1+z_L)D_0}\right]^{1/2}\frac{\sqrt{|\mu|}\;\Delta\kappa\,D_L}{r_\perp} \sim \frac{10^{-6}\,{\rm rad}}{(1+z_L)^{1/2}}\left(\frac{\lambda}{1\,\mu{\rm m}}\right)^{1/2}\left(\frac{D_{\rm eff}}{1\,{\rm Gpc}}\right)^{1/2} \times \left(\frac{|\mu|}{10^4}\right)^{1/2}\left(\frac{\Delta_\kappa}{10^{-4}}\right)\left(\frac{r_\perp}{100\,{\rm au}}\right)^{-1}. \quad (46)$$

For a range of parameters relevant to this work, this correction is also unimportant.

ORCID iDs

Liang Dai https://orcid.org/0000-0003-2091-8946
Jordi Miralda-Escudé https://orcid.org/0000-0002-2316-8370

References

Aguilar, L. A., & White, S. 1985, ApJ, 295, 374
Angus, G. W., & Zhao, H. 2007, MNRAS, 375, 1146
Berezhiani, Z., & Khlopov, M. Y. 1990, SvJNP, 51, 739
Berezinsky, V., Dokuchaev, V., & Eroshenko, Y. 2006, PhRvD, 73, 063504
Binney, J., & Tremaine, S. 2011, Galactic Dynamics (Princeton, NJ: Princeton Univ. Press)
Bird, S., Cholis, I., Munoz, J. B., et al. 2016, PhRvL, 116, 201301
Borsányi, S., Fodor, Z., Guenther, J., et al. 2016, Natur, 539, 69
Bullock, J. S., Kolatt, T. S., Sigad, Y., et al. 2001, MNRAS, 321, 559
Buschmann, M., Foster, J. W., & Safdi, B. R. 2019, arXiv:1906.00967
Carr, B., Kühnel, F., & Sandstad, M. 2016, PhRvD, 94, 083504
Carr, B. J., & Hawking, S. W. 1974, MNRAS, 168, 399
Chen, W., Kelly, P. L., Diego, J. M., et al. 2019, ApJ, 881, 8
Chikashige, Y., Mohapatra, R. N., & Peccei, R. D. 1981, PhLB, 98, 265
Choi, K.-S., Nilles, H. P., Ramos-Sánchez, S., & Vaudrevange, P. K. 2009, PhLB, 675, 381
Churazov, E., Vikhlinin, A., Zhuravleva, I., et al. 2012, MNRAS, 421, 1123
Cicoli, M., Goodsell, M. D., & Ringwald, A. 2012, JHEP, 2012, 146
Clesse, S., & García-Bellido, J. 2017, PDU, 15, 142
Conlon, J. P. 2006, JHEP, 2006, 078

Cooray, A., & Sheth, R. K. 2002, PhR, 372, 1
Dai, L., Li, S.-S., Zackay, B., Mao, S., & Lu, Y. 2018a, PhRvD, 98, 104029
Dai, L., Venumadhav, T., Kaurov, A. A., & Miralda-Escudé, J. 2018b, ApJ, 867, 24
Dai, X., & Guerras, E. 2018, ApJL, 853, L27
Davidson, S., & Schwetz, T. 2016, PhRvD, 93, 123509
Despali, G., Vegetti, S., White, S. D. M., Giocoli, C., & van den Bosch, F. C. 2018, MNRAS, 475, 5424
Dias, A., Machado, A., Nishi, C., Ringwald, A., & Vaudrevange, P. 2014, JHEP, 2014, 37
di Cortona, G. G., Hardy, E., Vega, J. P., & Villadoro, G. 2016, JHEP, 2016, 34
Diego, J. M. 2019, A&A, 625, A84
Diego, J. M., Kaiser, N., Broadhurst, T., et al. 2018, ApJ, 857, 25
Diemand, J., Kuhlen, M., & Madau, P. 2006, ApJ, 649, 1
Diemand, J., Moore, B., & Stadel, J. 2005, Natur, 433, 389
Diemer, B. 2018, ApJS, 239, 35
Diemer, B., & Joyce, M. 2018, ApJ, 871, 168
Dine, M., Fischler, W., & Srednicki, M. 1981, PhLB, 104, 199
Efstathiou, G., & Bond, J. R. 1986, MNRAS, 218, 103
Enander, J., Pargner, A., & Schwetz, T. 2017, JCAP, 1712, 038
Fairbairn, M., Marsh, D. J., Quevillon, J., & Rozier, S. 2018, PhRvD, 97, 083502
Fairbairn, M., Marsh, D. J. E., & Quevillon, J. 2017, PhRvL, 119, 021101
García-Bellido, J. 2017, JPhCS, 840, 012032
Gaspari, M., Churazov, E., Nagai, D., Lau, E. T., & Zhuravleva, I. 2014, A&A, 569, A67
Gelmini, G. B., & Roncadelli, M. 1981, PhLB, 99, 411
Georgi, H. M., Hall, L. J., & Wise, M. B. 1981, NuPhB, 192, 409
Goerdt, T., Gnedin, O. Y., Moore, B., Diemand, J., & Stadel, J. 2007, MNRAS, 375, 191
Green, A. M., & Goodwin, S. P. 2007, MNRAS, 375, 1111
Gross, D. J., Pisarski, R. D., & Yaffe, L. G. 1981, RvMP, 53, 43
Hardy, E. 2017, JHEP, 2017, 46
Hawking, S. 1971, MNRAS, 152, 75
Hogan, C., & Rees, M. 1988, PhLB, 205, 228
Husdal, L. 2016, Galax, 4, 78
Inman, D., & Ali-Haïmoud, Y. 2019, PhRvD, 100, 083528
Inomata, K., Kawasaki, M., Kusenko, A., & Yang, L. 2018, JCAP, 1812, 003
Inomata, K., Kawasaki, M., & Tada, Y. 2016, PhRvD, 94, 043527
Jaeckel, J. 2014, PhLB, 732, 1
Jeong, D., Pradler, J., Chluba, J., & Kamionkowski, M. 2014, PhRvL, 113, 061301
Kaurov, A. A., Dai, L., Venumadhav, T., Miralda-Escudé, J., & Frye, B. 2019, ApJ, 880, 58
Kawahara, H., Reese, E. D., Kitayama, T., Sasaki, S., & Suto, Y. 2008, ApJ, 687, 936
Kawamata, R., Oguri, M., Ishigaki, M., Shimasaku, K., & Ouchi, M. 2016, ApJ, 819, 114
Kelly, P. L., Diego, J. M., Rodney, S., et al. 2018, NatAs, 2, 334
Kibble, T. W. 1976, JPhA, 9, 1387
Kim, J. E. 1979, PhRvL, 43, 103
Kolb, E. W., & Tkachev, I. I. 1994, PhRvD, 50, 769
Kolb, E. W., & Tkachev, I. I. 1996, ApJL, 460, L25
Luan, J., & Goldreich, P. 2014, ApJL, 785, L26
Ludlow, A. D., Navarro, J. F., Boylan-Kolchin, M., et al. 2013, MNRAS, 432, 1103
Ma, C.-P., & Bertschinger, E. 1995, ApJ, 455, 7
Minor, Q. E., Kaplinghat, M., & Li, N. 2017, ApJ, 845, 118
Montero-Camacho, P., Fang, X., Vasquez, G., Silva, M., & Hirata, C. M. 2019, JCAP, 08, 031
Mróz, P., Udalski, A., Skowron, J., et al. 2017, Natur, 548, 183
Navarro, J. F., Frenk, C. S., & White, S. D. 1997, ApJ, 490, 493
Navarro, J. F., Frenk, C. S., & White, S. D. M. 1996, ApJ, 462, 563
Oguri, M., Diego, J. M., Kaiser, N., Kelly, P. L., & Broadhurst, T. 2018, PhRvD, 97, 023518
Peccei, R. D., & Quinn, H. R. 1977, PhRvD, 16, 1791
Pendlebury, J. M., Afach, S., Ayres, N. J., et al. 2015, PhRvD, 92, 092003
Press, W. H., & Schechter, P. 1974, ApJ, 187, 425
Sasaki, M., Suyama, T., Tanaka, T., & Yokoyama, S. 2016, PhRvL, 117, 061101
Schneider, A., Krauss, L., & Moore, B. 2010, PhRvD, 82, 063525
Schuecker, P., Finoguenov, A., Miniati, F., Bohringer, H., & Briel, U. G. 2004, A&A, 426, 387
Shifman, M. A., Vainshtein, A., & Zakharov, V. I. 1980, NuPhB, 166, 493
Sumi, T., Kamiya, K., Bennett, D. P., et al. 2011, Natur, 473, 349
Tinyakov, P., Tkachev, I., & Zioutas, K. 2016, JCAP, 1601, 035
Vaquero, A., Redondo, J., & Stadler, J. 2019, JCAP, 04, 012
Venumadhav, T., Dai, L., & Miralda-Escudé, J. 2017, ApJ, 850, 49
Weinberg, S. 1978, PhRvL, 40, 223
Wilczek, F. 1978, PhRvL, 40, 279
Wilczek, F. 1982, PhRvL, 49, 1549
Windhorst, R. A., Timmes, F., Wyithe, J. S. B., et al. 2018, ApJS, 234, 41
Witten, E. 1984, PhLB, 149, 351
Zel'dovich, Y. B., & Novikov, I. 1967, SvA, 10, 602
Zhao, D., Jing, Y., Mo, H., & Börner, G. 2009, ApJ, 707, 354
Zhao, D.-H., Jing, Y., Mo, H., & Börner, G. 2003, ApJL, 597, L9
Zhao, H., Taylor, J. E., Silk, J., & Hooper, D. 2007, ApJ, 654, 697